

©Copyright 2023

Anthony Su

Modeling of Active Aerostervoelastic Systems

Anthony Su

A thesis
submitted in partial fulfillment of the
requirements for the degree of

Master of Science in Aeronautics & Astronautics

University of Washington

2023

Committee:

Eli Livne, Chair

Ed Habtour

Program Authorized to Offer Degree:

William E. Boeing Department of Aeronautics & Astronautics

University of Washington

Abstract

Modeling of Active Aeroservoelastic Systems

Anthony Su

Chair of the Supervisory Committee:

Professor Eli Livne

William E. Boeing Department of Aeronautics & Astronautics

This thesis demonstrates the synthesis and testing of a physics-based aeroservoelastic mathematical model for a flexible wind tunnel model. Ground vibration testing of the wind tunnel model is detailed herein. An aeroservoelastic mathematical model was synthesized for the wind tunnel model from a finite-element analysis and first principles. The wind tunnel model's structural dynamic, aerodynamic, and actuator models were coupled together into a linear time-invariant state-space model. The wind tunnel model's frequency response was measured experimentally at the University of Washington's 3x3 low-speed wind tunnel. The frequency response was used to adjust the mathematical model to account for physical phenomena which were not well captured by the initial model. Results show that the updated mathematical model is able to capture the relevant physics and responses of the wind tunnel model. The results of this study can be used as the baseline for further system identification or for aeroservoelastic control law design.

TABLE OF CONTENTS

	Page
List of Figures	iv
List of Tables	v
Nomenclature	vi
Chapter 1: Introduction	1
1.1 Background	1
1.2 Contribution	2
1.3 Organization	2
Chapter 2: System Description	3
Chapter 3: Dynamic System Modeling	7
3.1 Plant Dynamics	7
3.1.1 Structural Dynamics	7
3.1.2 The Roger Approximation	9
3.1.3 Coupled Aeroelastic Dynamics	11
3.2 Plant Output Modeling	16
3.2.1 Acceleration Output	17
3.2.2 Pitch Output	18
3.2.3 Strain Output	18
3.3 Actuation and Sensing Dynamics	20
3.3.1 Control Surfaces	20
3.3.2 Gust Vanes	21
3.3.3 Combined Actuation and Sensing	22
3.4 Coupled Aeroservoelastic Modeling	23

Chapter 4: Finite Element Modeling	26
Chapter 5: Ground Vibration Testing	30
5.1 Experiment	30
5.1.1 Test Setup	30
5.1.2 Test Procedure	32
5.2 Generating Frequency Response Functions	33
5.2.1 Time-Domain Post-Processing	33
5.2.2 Computing Frequency Response Functions	34
5.3 Determining Modal Properties	36
5.3.1 Computing Natural Frequencies	36
5.3.2 Computing Damping Ratios	37
5.4 Finite Element Model Correction	37
Chapter 6: Wind Tunnel Testing	41
6.1 Data Postprocessing	42
6.1.1 Accelerometer Data Postprocessing	42
Chapter 7: Model Tuning and Results	44
7.1 Tuning Parameters	44
7.2 Manual Model Tuning	48
7.3 Model Optimization	51
7.3.1 Computing FRF Error	51
7.3.2 Design Variable Bounds	52
7.3.3 Optimization Results	53
Chapter 8: Conclusion	58
8.1 Future Work	58
Bibliography	60
Appendix A: Frequency Response Plots	62
A.1 Ground Vibration Testing	62
A.2 Wind Tunnel Testing and Mathematical Models	71

Appendix B: optModel	78
--------------------------------	----

LIST OF FIGURES

Figure Number	Page
2.1 MARGE structural configuration	4
2.2 MARGE sensing and actuation configuration	5
2.3 Univeristy of Washington 3x3 low-speed wind tunnel	6
3.1 Bode plot of actuator transfer function	21
3.2 Padé approximant of the pure-delay response of the wind tunnel gust vanes .	22
3.3 Integrated model of actuation, plant, and sensing in a control loop	24
4.1 NASTRAN finite-element model of MARGE, gust vanes, and wind tunnel walls	28
4.2 NASTRAN finite-element model, close-up of MARGE only	29
5.1 Accelerometer placement in ground vibration testing of MARGE	31
5.2 Example GVT time-series data from an impulse at the location 2214z	33
5.3 Example GVT frequency response data from an impulse at the location 2214z to an accelerometer at the location 2314z	35
5.4 Finite-element model material parameter adjustment	38
6.1 Sample wind tunnel time-series data from a single run	42
7.1 A comparison of experimental FRFs and untuned model FRFs at $q = 207$ Pa. The grey region is enclosed by the experimental H_1 FRF below and the experimental H_2 FRF above.	47
7.2 A comparison of experimental FRFs and manually-tuned model FRFs. The grey region is enclosed by the experimental H_1 FRF below and the experi- mental H_2 FRF above.	50

LIST OF TABLES

Table Number	Page
4.1 Properties of Beam Finite Elements	26
4.2 NASTRAN Modal Properties	27
5.1 Finite-Element Model Material Parameter Adjustment	37
5.2 Experimental Natural Modes	39
5.3 Natural Frequencies of Uncorrected FEM, Corrected FEM, and Experiment .	40
7.1 Default Values of MARGE Tuning Parameters	46
7.2 Manually Tuned Values of MARGE Tuning Parameters	49
7.3 Bounds of MARGE Tuning Parameter Design Variables	53
7.5 Select Model Tuning Optimized Parameters	54
7.4 Model Tuning Optimization Results	55

NOMENCLATURE

Notation

[]	=	matrix
{ }	=	column vector

Abbreviations

CZT	=	chirp Z-transform
DFT	=	discrete Fourier transform
FEM	=	finite element model
FRF	=	frequency response function
GLA	=	gust load alleviation
GVT	=	ground vibration testing
HIL	=	hardware-in-the-loop
LE	=	leading edge
MARGE	=	Model for Aeroelastic Response to Gust Excitation
ODE	=	ordinary differential equation
SISO	=	single-input single-output
TE	=	trailing edge

Variables

b	=	reference semi-chord
j	=	imaginary unit
k	=	reduced frequency
N_s	=	# of elastic modes available
n_s	=	# of elastic modes used in modeling

n_c	=	# of rigid-body modes used in modeling
n_{lag}	=	# of lag terms used in modeling
q_D	=	dynamic pressure
s	=	Laplace variable
U	=	airspeed
ω	=	frequency

Subscripts

s	=	structural (flexible) component
c	=	control (rigid) component
p	=	plant
act	=	actuator
sens	=	sensor

ACKNOWLEDGMENTS

I must first and foremost thank Professor Eli Livne for his mentorship and support throughout my foray into aeroservoelasticity. His passion for aeronautics has proven to be contagious and for that I am grateful. I would like to thank colleagues John Berg and Eddie Ting for their enduring patience and readiness to lend experience. Thanks also to Professor Marat Mor for his invaluable expertise and assistance in finite-element modeling; this work would not have been possible without him. Thanks to the members of the UW Illimited lab for generously lending me their equipment. Finally, I would like to thank all of the colleagues, friends, and family who have walked alongside me throughout my educational journey.

Chapter 1

INTRODUCTION

1.1 *Background*

Active aeroservoelastic control is a key tool in the pursuit of increased aircraft performance. Applications of active control include ride comfort improvement ([1]), maneuver load alleviation ([8]), gust load alleviation ([3]), and flutter suppression ([2]). Suchs technologies can result in reduced structural weight, increased passenger comfort, or improved handling qualities, all of which lead to a better performing aircraft.

Determination of the aircraft's mathematical model is a prerequisite to designing these aeroservoelastic control laws. The mathematical model must capture the relevant physics of the aircraft in order for the control laws designed around it to function properly when implemented. These mathematical models can be determined using analytical modeling, experimental data, or both.

System identification from experimental data can be done via black-box system identification (where the mathematical model's structure is arbitrary) or grey-box system identification (where the mathematical model's structure is pre-determined). Unlike mathematical models from black-box system identification, physics-based grey-box mathematical models are capable of generalizing to conditions outside of those from which they were derived. Such a generalizable mathematical model is desirable for aeroservoelastic systems because it expands the validity of the model to flight conditions outside of those it was explicitly tested in, significantly reducing the cost of testing in order to cover all relevant flight conditions.

1.2 Contribution

This thesis describes of the modeling methods and experimental validation work performed to synthesize one such grey-box aeroservoelastic mathematical model for a wind tunnel model named MARGE [5]. The mathematical model takes the form of a linear, time-invariant state-space equation which is amenable for use in the design of aeroservoelastic flight control laws. This mathematical model is based on both analytical modeling and experimental data. The experiments performed include ground vibration testing and wind tunnel testing. The analytical model is augmented using the experimental data to better match the behavior of the wind tunnel model.

1.3 Organization

The remainder of this thesis is organized as follows: first, the test article used in this study is described in Chapter 2. Then, the modeling methods used to generate the state-space model are formulated in Chapter 3. The finite-element model and the GVT done to correct it are covered in Chapters 4 and 5, respectively. The wind tunnel testing and model tuning performed based on it are covered in Chapters 6 and 7, respectively. Finally, Chapter 8 concludes with a discussion of the results and potential follow-on studies.

Chapter 2

SYSTEM DESCRIPTION

The subject of this study's modeling effort is the Model for Aeroelastic Response to Gust Excitation (MARGE). MARGE is a flexible half-span wing-body-tail wind tunnel model which is capable of rigid-body rotation in the pitch axis. It was designed to allow rapid and accessible testing of gust alleviation control laws. Thus, it is of a simple and affordable construction. Details of the original design and construction of MARGE can be found in [5].

The structure of MARGE consists of flexible beams encapsulated by lightweight aerodynamic shells. The wing and tail spars are made of aluminum while the fuselage is made of steel. The aerodynamic shells are made of polylactic acid (PLA) and form a symmetrical NACA 0012 airfoil. There is a brass mass fixed at the wing tip to bring the structure's natural frequencies to the designed magnitude. The wing is joined to the fuselage at its root and the entire assembly rotates about a shaft which is suspended from the hanging sub-assembly by bearings. A diagram of the structural configuration of MARGE is shown in Fig. 2.1.

MARGE has three actuators: two servo-actuated control surfaces on the wing and one servo-actuated elevator on the tail. There are also two servo-activated gust vanes installed upstream of the test section in the 3x3 low-speed wind tunnel. The gust vanes move in unison to generate discrete or continuous gusts and are controlled as a single actuator.

MARGE has five sensors. There are two unidirectional accelerometers at the wingtip, one ahead of the wing spar and one aft of the wing spar. There is another unidirectional accelerometer at the tip of the tail. (All three accelerometers are aligned normal to the lifting surfaces.) There is a strain gauge at the wing root. Finally, there is a hall effect sensor inside the hanging sub-assembly by the model's rotating shaft. There is a magnet fixed to the shaft which allows the hall effect sensor to measure the rotation of the shaft. A diagram of the

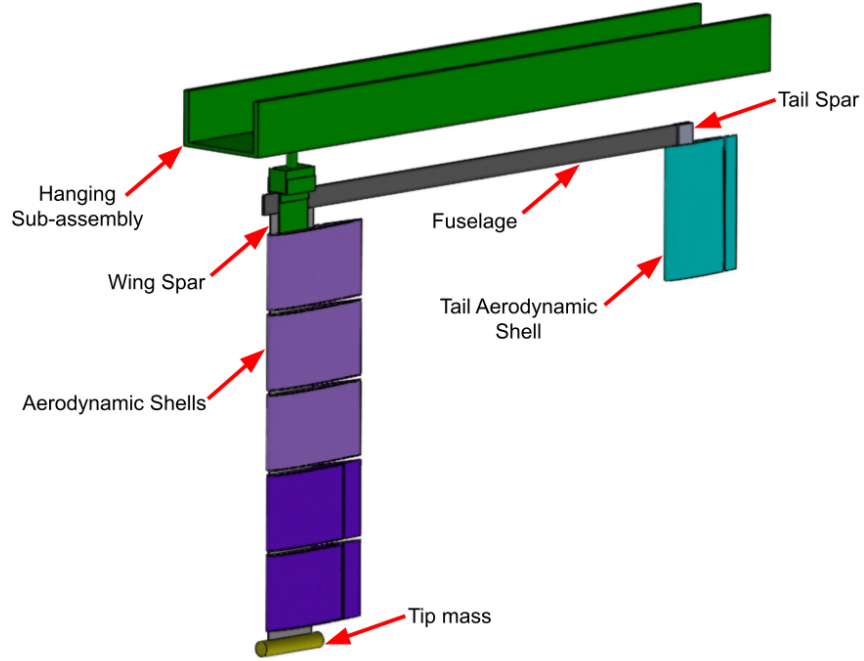


Figure 2.1: MARGE structural configuration

sensing and actuation configuration of MARGE is shown in Fig. 2.2.

Note that the sensor configuration is modified from the original design specified in [5]. The original design featured potentiometers on the control surfaces and a strain gauge on the fuselage. It also lacked the accelerometer on the tail. The accelerometer on the tail was since added with the intent of capturing fuselage and tail flexible motions.

MARGE is designed to fit into the University of Washington's 3x3 low-speed wind tunnel. The 3x3 low-speed wind tunnel is an open-loop wind tunnel capable of speeds up to 60 m/s. The wind tunnel has flow straighteners, a 9:1 contraction, gust vanes, and a 3 ft. by 3 ft. by 8 ft. test section. Further details about the 3x3 low-speed wind tunnel can be found in [4]. When installed, MARGE hangs vertically from the ceiling of the test section. A diagram indicating the key features of the 3x3 low-speed wind tunnel is shown in Fig. 2.3.

The physical interface to MARGE's acutation and sensing is a National Instruments

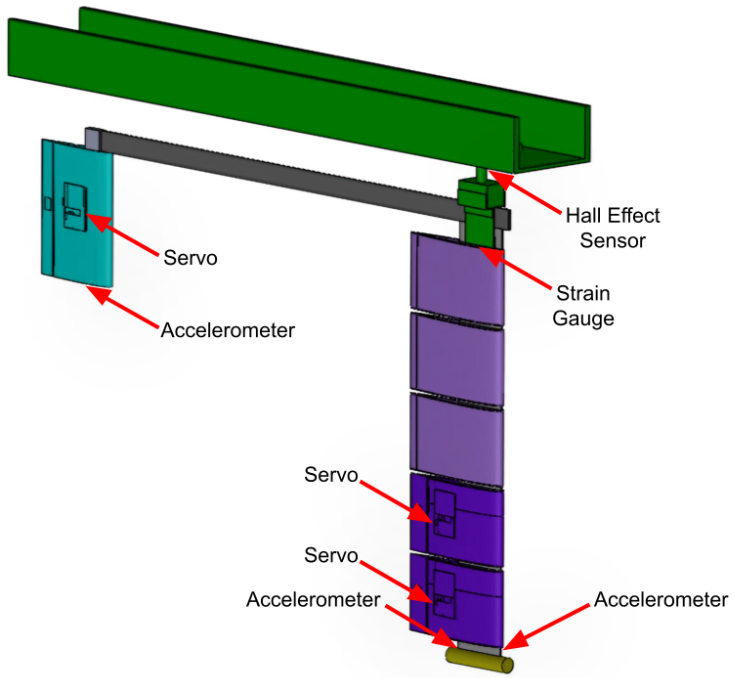


Figure 2.2: MARGE sensing and actuation configuration

DAQ coupled with a National Instruments terminal block. The exceptions to this are the gust vanes, which are controlled through HTTP on the local network. Data is transmitted and received to and from these interfaces through Simulink Real-Time.

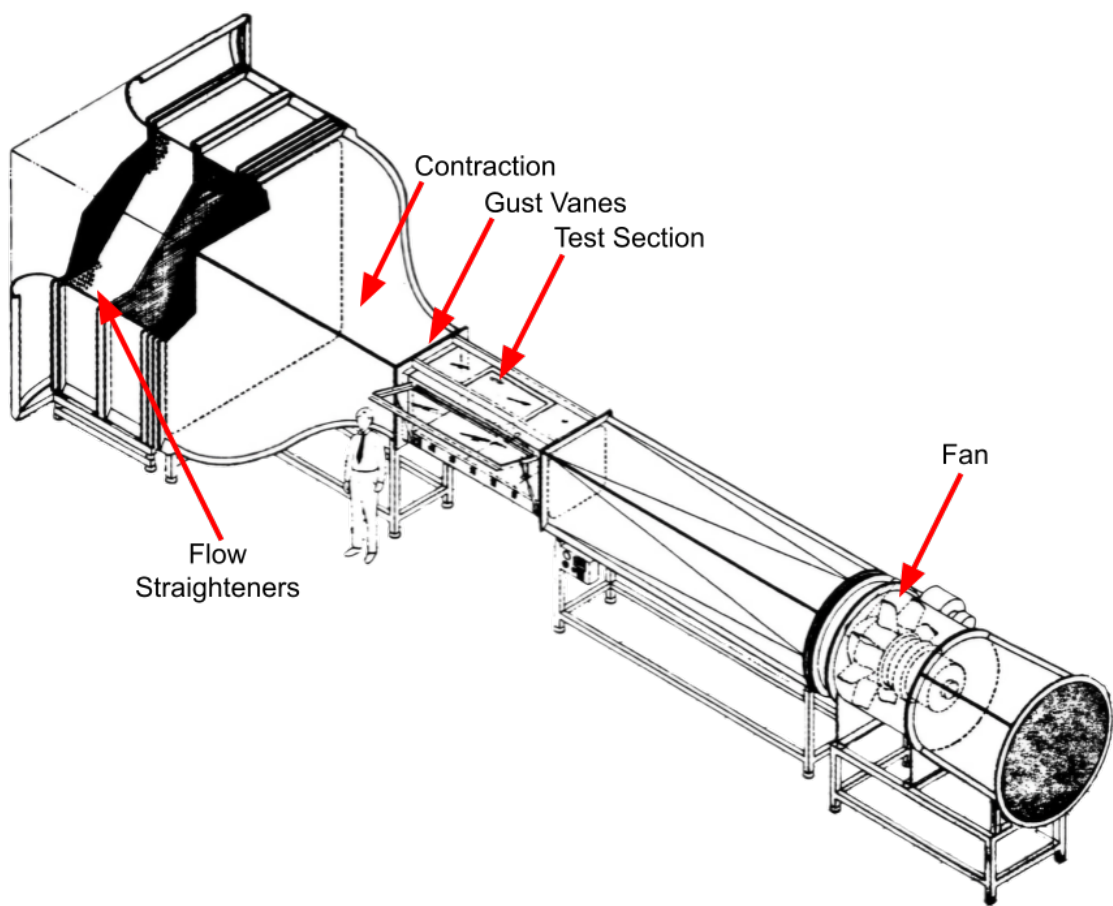


Figure 2.3: Univeristy of Washington 3x3 low-speed wind tunnel

Chapter 3

DYNAMIC SYSTEM MODELING

The goal of this chapter is to derive a preliminary state-space model for MARGE in the form

$$\begin{aligned}s\{x\} &= [A]\{x\} + [B]\{u\} \\ \{y\} &= [C]\{x\} + [D]\{u\}\end{aligned}\tag{3.1}$$

based on first principles.

3.1 Plant Dynamics

This section will derive the plant dynamics for MARGE in the form

$$s\{x\} = [A_p]\{x_p\} + [B_p]\{u_p\}\tag{3.2}$$

3.1.1 Structural Dynamics

MARGE's structure is modeled as a linear, second-order system with damping and external forcing. The equations of motion for such a system are

$$s^2[M]\{q(s)\} + s[C]\{q(s)\} + [K]\{q(s)\} = \{f(s)\}\tag{3.3}$$

where $\{q\}$ is the structural dynamic state expressed in generalized modal coordinates, $\{f(s)\}$ is the generalized external forcing, and $[M]$, $[C]$, and $[K]$ are generalized mass, damping, and stiffness matrices respectively. Note that the modal coordinates include both elastic motions (of the structure) denoted by the subscript s and rigid-body motions (of the structure and the control surfaces) denoted by the subscript c :

$$\{q\} = \begin{Bmatrix} q_s \\ q_c \end{Bmatrix}\tag{3.4}$$

The forcing for the aeroservoelastic wing can be decomposed into the aerodynamic forcing due to the state and the forcing from actuator hinge moments:

$$s^2[M]\{q(s)\} + s[C]\{q(s)\} + [K]\{q(s)\} = q_D[A(s)]\{q(s)\} + \begin{Bmatrix} \{0\} \\ \{H_c\} \end{Bmatrix} \quad (3.5)$$

where $[A(s)]$ is the aerodynamic influence matrix for the state and $\{H_c\}$ are the hinge moments from the actuators.

The whole system can be further decomposed into structural and control components:

$$\begin{aligned} & \left(s^2 \begin{bmatrix} [M_{ss}] & [M_{sc}] \\ [M_{cs}] & [M_{cc}] \end{bmatrix} + s \begin{bmatrix} [C_{ss}] & [C_{sc}] \\ [C_{cs}] & [C_{cc}] \end{bmatrix} + \begin{bmatrix} [K_{ss}] & [K_{sc}] \\ [K_{cs}] & [K_{cc}] \end{bmatrix} \right) \begin{Bmatrix} \{q_s(s)\} \\ \{q_c(s)\} \end{Bmatrix} \\ &= q_D \begin{bmatrix} [A_{ss}(s)] & [A_{sc}(s)] \\ [A_{cs}(s)] & [A_{cc}(s)] \end{bmatrix} \begin{Bmatrix} \{q_s(s)\} \\ \{q_c(s)\} \end{Bmatrix} + \begin{Bmatrix} \{0\} \\ \{H_c\} \end{Bmatrix} \end{aligned} \quad (3.6)$$

The control modes are those corresponding to rigid-body motions of control surfaces. The structural modes are all other modes, including flexible-body modes and rigid-body pitching of the entire model.

It is assumed that the dynamics of the control modes are completely determined by the control inputs and the inputs are not directly affected by the control modes, i.e. the actuators are irreversible controls. Then, interest is only in the dynamics of the structural modes:

$$\begin{aligned} & \left(s^2 \begin{bmatrix} [M_{ss}] & [M_{sc}] \end{bmatrix} + s \begin{bmatrix} [C_{ss}] & [C_{sc}] \end{bmatrix} + \begin{bmatrix} [K_{ss}] & [K_{sc}] \end{bmatrix} \right) \begin{Bmatrix} \{q_s(s)\} \\ \{q_c(s)\} \end{Bmatrix} \\ &= q_D \begin{bmatrix} [A_{ss}(s)] & [A_{sc}(s)] \end{bmatrix} \begin{Bmatrix} \{q_s(s)\} \\ \{q_c(s)\} \end{Bmatrix} \end{aligned} \quad (3.7)$$

Note that since the control modes are rigid-body modes, they have no stiffness and the

equations of motion further simplify to

$$\begin{aligned} & \left(s^2 \begin{bmatrix} [M_{ss}] & [M_{sc}] \end{bmatrix} + s \begin{bmatrix} [C_{ss}] & [C_{sc}] \end{bmatrix} + \begin{bmatrix} [K_{ss}] & [0] \end{bmatrix} \right) \begin{Bmatrix} \{q_s(s)\} \\ \{q_c(s)\} \end{Bmatrix} \\ &= qD \begin{bmatrix} [A_{ss}(s)] & [A_{sc}(s)] \end{bmatrix} \begin{Bmatrix} \{q_s(s)\} \\ \{q_c(s)\} \end{Bmatrix} \quad (3.8) \end{aligned}$$

3.1.2 The Roger Approximation

The aerodynamic influence matrix $[A]$ is a function of the Laplace variable s . For a thin airfoil oscillating in a potential flow, Theodorsen's analytical solution applies [10]. In the more general case of an aircraft's wing in three dimensions, a numerical solver using doublet-lattice theory can compute $[A]$. This solution is nonlinear and unable to be represented in a linear system. In order to obtain the linear state-space system, $[A]$ must be approximated as an analytic function of s .

The Roger approximation [7] is a method of generating a rational function approximation of the aerodynamic influence matrix in the form

$$[A(s)] \approx [P_0] + s[P_1] + s^2[P_2] + \sum_{n=1}^{N_{\text{lag}}} \frac{s}{s + \beta_n} [P_{n+2}] \quad (3.9)$$

where $[P]$ are the unknown real-valued matrices that are fit to tabulated known $[A(s)]$ matrices (obtained from an unsteady aerodynamic solver such as that found in NASTRAN). Aside from the zeroth, first, and second order terms, there are N_{lag} additional “lag term” approximating functions which are defined by their respective constants β . These constants β are chosen by the user.

Begin with an approximation only along the frequency domain:

$$[A(jk)] \approx [\bar{P}_0] + jk[\bar{P}_1] + (jk)^2[\bar{P}_2] + \sum_{n=1}^{N_{\text{lag}}} \frac{jk}{jk + \bar{\beta}_n} [\bar{P}_{n+2}] \quad (3.10)$$

where k is the reduced frequency

$$k = \frac{\omega \cdot b}{U} \quad (3.11)$$

Given the tabulated set of aerodynamic influence matrices $[A]$ computed across N reduced frequencies, each entry p of the matrices $[\bar{P}]$ in the above approximation can be fit to the corresponding entries a of the aerodynamic influence matrices $[A]$. The steady-state component of the approximation $[\bar{P}_0]$ is fixed to be equal to the steady-state aerodynamic influence matrix (with zero reduced frequency):

$$[\bar{P}_0] = [A(k = 0)] \quad (3.12)$$

The remaining $[\bar{P}]$ matrices are determined using a linear regression:

$$\begin{bmatrix} 0 & -k_1^2 & \frac{k_1^2}{k_1^2 + \bar{\beta}_1^2} & \cdots & \frac{k_1^2}{k_1^2 + \bar{\beta}_{N_{\text{lag}}}^2} \\ k_1 & 0 & \frac{k_1 \bar{\beta}_1}{k_1^2 + \bar{\beta}_1^2} & \cdots & \frac{k_1 \bar{\beta}_1}{k_1^2 + \bar{\beta}_{N_{\text{lag}}}^2} \\ \vdots & \vdots & \vdots & & \vdots \\ 0 & -k_N^2 & \frac{k_N^2}{k_N^2 + \bar{\beta}_1^2} & \cdots & \frac{k_N^2}{k_N^2 + \bar{\beta}_{N_{\text{lag}}}^2} \\ k_N & 0 & \frac{k_N \bar{\beta}_1}{k_N^2 + \bar{\beta}_1^2} & \cdots & \frac{k_N \bar{\beta}_1}{k_N^2 + \bar{\beta}_{N_{\text{lag}}}^2} \end{bmatrix} \begin{Bmatrix} \bar{p}_1 \\ \vdots \\ \bar{p}_{N_{\text{lag}}+2} \end{Bmatrix} = \begin{Bmatrix} \text{Re}(a(jk_1)) - a(0) \\ \text{Im}(a(jk_1)) \\ \vdots \\ \text{Re}(a(jk_N)) - a(0) \\ \text{Im}(a(jk_N)) \end{Bmatrix} \quad (3.13)$$

The linear regression in Eq. 3.13 can then be solved using the method of least-squares to obtain the fitted $[\bar{P}]$ matrices.

Replacing the reduced frequency with the equivalent angular frequency yields

$$[A(j\omega)] \approx [P_0] + j\omega[P_1] - \omega^2[P_2] + \sum_{n=1}^{N_{\text{lag}}} \frac{j\omega}{j\omega + \beta_n} [P_{n+2}] \quad (3.14)$$

where

$$\begin{aligned}
[P_0] &= [\bar{P}_0] \\
[P_1] &= [\bar{P}_1] \frac{b}{U} \\
[P_2] &= [\bar{P}_2] \left(\frac{b}{U} \right)^2 \\
[P_3] &= [\bar{P}_3] \\
&\vdots \\
[P_{N_{\text{lag}}+2}] &= [\bar{P}_{N_{\text{lag}}+2}] \\
\beta_1 &= \bar{\beta}_1 \frac{U}{b} \\
&\vdots \\
\beta_{N_{\text{lag}}} &= \bar{\beta}_{N_{\text{lag}}} \frac{U}{b}
\end{aligned} \tag{3.15}$$

This is then extended from the imaginary axis to the full Laplace domain through analytic continuation, leading to the final form of the Roger approximation for aerodynamic influence matrices:

$$[A(s)] \approx [P_0] + s[P_1] + s^2[P_2] + \sum_{n=1}^{N_{\text{lag}}} \frac{s}{s + \beta_n} [P_{n+2}] \tag{3.16}$$

It should be noted that the Roger approximation is only valid over the tabulated reduced frequency range. Thus, any result from the model is only valid if the airspeed that the model is analyzed at is sufficiently above

$$U_{\min} = \frac{\omega_{\max} \cdot b}{k_{\max}} \tag{3.17}$$

where ω_{\max} is the maximum frequency of interest in the analysis. Thus, modeling which utilizes the Roger Approximation cannot be used for purely structural dynamic analysis (where $U = 0$).

3.1.3 Coupled Aeroelastic Dynamics

This section describes how the structural dynamic equations of motion can be reduced to the form in Eq. 3.2.

Replacing the aerodynamic influence matrices in Eq. 3.8 with the equivalent Roger approximation and collecting like terms yields

$$\begin{aligned} & \left(s^2[M_{ss}] + s[C_{ss}] + [K_{ss}] - q_D \left([P_{ss,0}] + s[P_{ss,1}] + s^2[P_{,2}] + \sum_{n=1}^{N_{\text{lag}}} \frac{s}{s+\beta_n} [P_{ss,n+2}] \right) \right) \{q_s(s)\} \\ & = - \left(s^2[M_{sc}] + s[C_{sc}] - q_D \left([P_{sc,0}] + s[P_{sc,1}] + s^2[P_{sc,2}] + \sum_{n=1}^{N_{\text{lag}}} \frac{s}{s+\beta_n} [P_{sc,n+2}] \right) \right) \{q_c(s)\} \end{aligned} \quad (3.18)$$

Define the following coupled aeroelastic mass, damping, and stiffness matrices:

$$\begin{aligned} \left[\bar{\bar{M}} \right] &= [M] - q_D[P_2] \\ \left[\bar{\bar{C}} \right] &= [C] - q_D[P_1] \\ \left[\bar{\bar{K}} \right] &= [K] - q_D[P_0] \end{aligned} \quad (3.19)$$

Equation 3.18 then simplifies to

$$\begin{aligned} & \left(s^2 \left[\bar{\bar{M}}_{ss} \right] + s \left[\bar{\bar{C}}_{ss} \right] + \left[\bar{\bar{K}}_{ss} \right] \right) \{q_s(s)\} - q_D \left(\sum_{n=1}^{N_{\text{lag}}} \frac{s}{s+\beta_n} [P_{ss,n+2}] \right) \{q_s(s)\} \\ & = - \left(s^2 \left[\bar{\bar{M}}_{sc} \right] + s \left[\bar{\bar{C}}_{sc} \right] + \left[\bar{\bar{K}}_{sc} \right] \right) \{q_c(s)\} + q_D \left(\sum_{n=1}^{N_{\text{lag}}} \frac{s}{s+\beta_n} [P_{sc,n+2}] \right) \{q_c(s)\} \end{aligned} \quad (3.20)$$

Rearranging the lag terms,

$$\begin{aligned} & \left(s^2 \left[\bar{\bar{M}}_{ss} \right] + s \left[\bar{\bar{C}}_{ss} \right] + \left[\bar{\bar{K}}_{ss} \right] \right) \{q_s(s)\} \\ & - q_D \begin{bmatrix} \sum_{n=1}^{N_{\text{lag}}} \frac{s}{s+\beta_n} [P_{ss,n+2}] & \sum_{n=1}^{N_{\text{lag}}} \frac{s}{s+\beta_n} [P_{sc,n+2}] \end{bmatrix} \begin{Bmatrix} q_s(s) \\ q_c(s) \end{Bmatrix} \\ & = - \left(s^2 \left[\bar{\bar{M}}_{sc} \right] + s \left[\bar{\bar{C}}_{sc} \right] + \left[\bar{\bar{K}}_{sc} \right] \right) \{q_c(s)\} \end{aligned} \quad (3.21)$$

Define the following aerodynamic ‘‘lag states’’ as

$$\begin{aligned}\{r_1\} &= \begin{bmatrix} [P_{ss,3}] & [P_{sc,3}] \end{bmatrix} \frac{s}{s + \beta_1} \\ &\vdots \\ \{r_{N_{\text{lag}}}\} &= \begin{bmatrix} [P_{ss,N_{\text{lag}}+2}] & [P_{sc,N_{\text{lag}}+2}] \end{bmatrix} \frac{s}{s + \beta_{N_{\text{lag}}}}\end{aligned}\quad (3.22)$$

Rearranging this yields an expression for the first derivative of the lag states:

$$\begin{aligned}s\{r_1\} &= s[P_{ss,3}]\{q_s(s)\} + s[P_{sc,3}]\{q_c(s)\} - \beta_1\{r_1\} \\ &\vdots \\ s\{r_{N_{\text{lag}}}\} &= s[P_{ss,N_{\text{lag}}+2}]\{q_s\} + s[P_{sc,N_{\text{lag}}+2}]\{q_c\} - \beta_{N_{\text{lag}}}\{r_{N_{\text{lag}}}\}\end{aligned}\quad (3.23)$$

Combining these lag state dynamic equations into a single matrix equation yields

$$s\{r\} = s[B_{rs}]\{q_s\} + s[B_{rc}]\{q_c\} + [A_r]\{r\} \quad (3.24)$$

where $\{r\}$, $[B_{rs}]$, $[B_{rc}]$, and $[A_r]$ are defined as

$$\begin{aligned}\{r\} &= \left\{ \begin{array}{c} \{r_1\} \\ \vdots \\ \{r_{N_{\text{lag}}}\} \end{array} \right\} \\ [B_{rs}] &= \begin{bmatrix} [P_{ss,3}] \\ \vdots \\ [P_{ss,N_{\text{lag}}+2}] \end{bmatrix} \\ [B_{rc}] &= \begin{bmatrix} [P_{sc,3}] \\ \vdots \\ [P_{sc,N_{\text{lag}}+2}] \end{bmatrix} \\ [A_r] &= \begin{bmatrix} -\beta_1[I] & & \\ & \ddots & \\ & & -\beta_{N_{\text{lag}}}[I] \end{bmatrix}\end{aligned}\quad (3.25)$$

With the lag states defined, Eq.3.21 can now be rewritten as

$$\begin{aligned} \left(s^2 \left[\bar{\bar{M}}_{ss} \right] + s \left[\bar{\bar{C}}_{ss} \right] + \left[\bar{\bar{K}}_{ss} \right] \right) \{q_s(s)\} - q_D \sum_{n=1}^{N_{\text{lag}}} \{r_n\} \\ = - \left(s^2 \left[\bar{\bar{M}}_{sc} \right] + s \left[\bar{\bar{C}}_{sc} \right] + \left[\bar{\bar{K}}_{sc} \right] \right) \{q_c(s)\} \end{aligned} \quad (3.26)$$

The sum of lag states can be simplified introducing the matrix $[I_r]$ such that

$$\{r_1\} + \dots + \{r_{N_{\text{lag}}}\} = \begin{bmatrix} [I] & \dots & [I] \end{bmatrix} \begin{Bmatrix} \{r_1\} \\ \vdots \\ \{r_{N_{\text{lag}}}\} \end{Bmatrix} = [I_r]\{r\} \quad (3.27)$$

This further compacts Eq. 3.26, which becomes

$$\begin{aligned} \left(s^2 \left[\bar{\bar{M}}_{ss} \right] + s \left[\bar{\bar{C}}_{ss} \right] + \left[\bar{\bar{K}}_{ss} \right] \right) \{q_s(s)\} - q_D [I_r]\{r\} \\ = - \left(s^2 \left[\bar{\bar{M}}_{sc} \right] + s \left[\bar{\bar{C}}_{sc} \right] + \left[\bar{\bar{K}}_{sc} \right] \right) \{q_c(s)\} \end{aligned} \quad (3.28)$$

Define new structural dynamic state vectors as

$$\{x_1\} = \{q\} \quad (3.29)$$

$$\{x_2\} = s\{q\} \quad (3.30)$$

Using these, Eq. 3.28 can be rewritten as a first-order linear ODE for $\{x_2\}$:

$$\begin{aligned} s\{x_2\} = - \left[\bar{\bar{M}}_{ss} \right]^{-1} \left[\bar{\bar{C}}_{ss} \right] \{x_2\} - \left[\bar{\bar{M}}_{ss} \right]^{-1} \left[\bar{\bar{K}}_{ss} \right] \{x_1\} + q_D \left[\bar{\bar{M}}_{ss} \right]^{-1} [I_r]\{r\} \\ - \left[\bar{\bar{M}}_{ss} \right]^{-1} \left(s^2 \left[\bar{\bar{M}}_{sc} \right] + s \left[\bar{\bar{C}}_{sc} \right] + \left[\bar{\bar{K}}_{sc} \right] \right) \{q_c(s)\} \end{aligned} \quad (3.31)$$

Rearranging,

$$\begin{aligned} s\{x_2\} = - \left[\bar{\bar{M}}_{ss} \right]^{-1} \left[\bar{\bar{C}}_{ss} \right] \{x_2\} - \left[\bar{\bar{M}}_{ss} \right]^{-1} \left[\bar{\bar{K}}_{ss} \right] \{x_1\} \\ + q_D \left[\bar{\bar{M}}_{ss} \right]^{-1} [I_r]\{r\} - \left[\bar{\bar{M}}_{ss} \right]^{-1} \left[\left[\bar{\bar{K}}_{sc} \right] \quad \left[\bar{\bar{C}}_{sc} \right] \quad \left[\bar{\bar{M}}_{sc} \right] \right] \begin{Bmatrix} \{q_c(s)\} \\ s\{q_c(s)\} \\ s^2\{q_c(s)\} \end{Bmatrix} \end{aligned} \quad (3.32)$$

Define the following simplifying matrices:

$$[T_{21}] = -\left[\bar{\bar{M}}_{ss}\right]^{-1}\left[\bar{\bar{K}}_{ss}\right] \quad (3.33)$$

$$[T_{22}] = -\left[\bar{\bar{M}}_{ss}\right]^{-1}\left[\bar{\bar{C}}_{ss}\right] \quad (3.34)$$

$$[T_{2r}] = q_D \left[\bar{\bar{M}}_{ss}\right]^{-1} [I_r] \quad (3.35)$$

$$[T_{2c}] = -\left[\bar{\bar{M}}_{ss}\right]^{-1} \left[\begin{bmatrix} \bar{\bar{K}}_{sc} \\ \bar{\bar{C}}_{sc} \\ \bar{\bar{M}}_{sc} \end{bmatrix} \right] \quad (3.36)$$

Equation 3.32 then simplifies to

$$s\{x_2\} = [T_{21}]\{x_1\} + [T_{22}]\{x_2\} + [T_{2r}]\{r\} + [T_{2c}]\{q_c\} \quad (3.37)$$

Now there exist first-order linear ODEs for the structural dynamic states (Eq. 3.32) and the aerodynamic lag states (Eq. 3.24) so the dynamics of the full system can be written in state-space form:

$$s \begin{Bmatrix} \{x_1\} \\ \{x_2\} \\ \{r\} \end{Bmatrix} = \begin{bmatrix} [0] & [I] & [0] \\ [T_{21}] & [T_{22}] & [T_{2r}] \\ [0] & [B_{rs}] & [A_r] \end{bmatrix} \begin{Bmatrix} \{x_1\} \\ \{x_2\} \\ \{r\} \end{Bmatrix} + \begin{bmatrix} [0] & [0] & [0] \\ [0] & T_{2c} & [0] \\ [0] & [B_{rc}] & [0] \end{bmatrix} \begin{Bmatrix} \{q_c\} \\ s\{q_c\} \\ s^2\{q_c\} \end{Bmatrix} \quad (3.38)$$

Define the state vector of the MARGE plant to be

$$\{x_p\} = \begin{Bmatrix} \{x_1\} \\ \{x_2\} \\ \{r\} \end{Bmatrix} \quad (3.39)$$

and the input vector of the MARGE plant to be

$$\{u_p\} = \begin{Bmatrix} \{q_c\} \\ s\{q_c\} \\ s^2\{q_c\} \end{Bmatrix} \quad (3.40)$$

Then, Eq. 3.38 can be written in the form that is desired:

$$s\{x_p\} = [A_p]\{x_p\} + [B_p]\{u_p\} \quad (3.41)$$

where $[A_p]$ and $[B_p]$ are the block matrices in Eq. 3.38.

3.2 Plant Output Modeling

This section will derive the output equations for MARGE in the form

$$\{y_p\} = [C_p]\{x_p\} + [D_p]\{u_p\} \quad (3.42)$$

The output of MARGE consists of three acceleration, one strain, and one pitch measurements. The plant output model to be presented here captures all of these as well as an optional pitch rate output. Thus,

$$\{u_p\} = \begin{Bmatrix} \text{acceleration 1} \\ \text{acceleration 2} \\ \text{acceleration 3} \\ \text{strain} \\ \text{rotation} \\ \text{rotation rate} \end{Bmatrix} \quad (3.43)$$

These outputs are the inputs to the sensors described in the next section.

The structural dynamic generalized state $\{q\}$ has modal coordinates which correspond to n_s mode shapes of the structure $\{\phi_1\}, \dots, \{\phi_{n_s}\}$. These modes shapes are in physical coordinates and are known from the structural dynamic solution of the finite-element model. The motion of the system in physical coordinates $\{z(t)\}$ is

$$\{z(t)\} = [\{\phi_1\} \ \dots \ \{\phi_{n_s}\}] \{q\} \quad (3.44)$$

For the i th degree of freedom (DOF) of the system, this is

$$z_i(t) = [\phi^i] \{q(t)\} \quad (3.45)$$

where $[\phi^i]$ contains the contribution to that DOF's motion from each mode:

$$[\phi^i] = [\phi_1^i \ \dots \ \phi_{n_s}^i] \quad (3.46)$$

The motion of the system can be expressed in terms of the full plant state vector defined in Eq. 3.39 as

$$\{z_i(t)\} = [\phi^i] [T_{\text{disp}}] \{x_p(t)\} \quad (3.47)$$

where $[T_{\text{disp}}]$ is a matrix which extracts the $\{x_1\}$ component of $\{x_p\}$:

$$[T_{\text{disp}}] = \begin{bmatrix} [I]_{n_s \times n_s} & [0]_{n_s \times n_s} & [0]_{n_s \times n_{\text{lag}}} \end{bmatrix} \quad (3.48)$$

Here, n_s is the number of elastic “structural” modes used, n_c is the number of rigid-body “control” modes used, and n_{lag} is the number of lag terms used in the model.

Similarly, the rates of the system’s motion at DOF i can be expressed using the $\{x_2\}$ component of the state vector $\{x_p\}$:

$$\frac{d\{z_i(t)\}}{dt} = [\phi^i] [T_{\text{vel}}] \{x_p(t)\} \quad (3.49)$$

where $[T_{\text{vel}}]$ is a matrix which extracts the $\{x_2\}$ component of $\{x_p\}$:

$$[T_{\text{vel}}] = \begin{bmatrix} [0]_{n_s \times n_s} & [I]_{n_s \times n_s} & [0]_{n_s \times n_{\text{lag}}} \end{bmatrix} \quad (3.50)$$

3.2.1 Acceleration Output

The system’s accelerations at DOF i can then be expressed as

$$\frac{d^2\{z_i(t)\}}{dt^2} = [\phi^i] [T_{\text{vel}}] \frac{d\{x_p(t)\}}{dt} \quad (3.51)$$

The derivative of $\{x_p(t)\}$ is contained in Eq. 3.38. Using that expression here yields

$$\frac{d^2\{z_i(t)\}}{dt^2} = [\phi^i] [T_{\text{vel}}] ([A_p] \{x_p\} + [B_p] \{u_p(t)\}) \quad (3.52)$$

For the three accelerometer locations (DOFs) on MARGE with corresponding modal motions $\{\phi_1\}$, $\{\phi_2\}$, and $\{\phi_3\}$, the accelerations experienced by the sensors are

$$\begin{Bmatrix} y_1(t) \\ y_2(t) \\ y_3(t) \end{Bmatrix} = \begin{bmatrix} [\phi^1] [T_{\text{vel}}][A_p] \\ [\phi^2] [T_{\text{vel}}][A_p] \\ [\phi^3] [T_{\text{vel}}][A_p] \end{bmatrix} \{x_p(t)\} + \begin{bmatrix} [\phi^1] [T_{\text{vel}}][B_p] \\ [\phi^2] [T_{\text{vel}}][B_p] \\ [\phi^3] [T_{\text{vel}}][B_p] \end{bmatrix} \{u_p(t)\} \quad (3.53)$$

3.2.2 Pitch Output

For the pitch output which is a measure of position instead of acceleration, Eq. 3.47 is used instead:

$$u_5(t) = [\phi^5] [T_{\text{disp}}] \{x_p(t)\} \quad (3.54)$$

The corresponding pitch rate output is similarly given by 3.49

$$u_6(t) = [\phi^5] [T_{\text{vel}}] \{x_p(t)\} \quad (3.55)$$

Note that the pitch rate output uses the same DOF in the mode shape (ϕ^5) as the pitch output.

3.2.3 Strain Output

The structural dynamic generalized state $\{q\}$ has modal coordinates which also correspond to the load (force or moment) at each DOF in each of n_s mode shapes of the structure $\{\psi_1\}, \dots, \{\psi_{n_s}\}$. (This is also known from the finite element model.) The loading state of the system in physical coordinates $\{L(t)\}$ is

$$\{L(t)\} = \begin{bmatrix} \{\psi_1\} & \dots & \{\psi_{n_s}\} \end{bmatrix} \{q(t)\} \quad (3.56)$$

For the i th DOF of the system,

$$L_i(t) = [\psi^i] \{q(t)\} \quad (3.57)$$

where

$$\psi^i = \begin{bmatrix} \psi_1^i & \dots & \psi_{n_s}^i \end{bmatrix} \{q(t)\} \quad (3.58)$$

In a similar fashion as in Eq. 3.47, this DOF's load can be expressed in terms of the system state:

$$\psi^i = \begin{bmatrix} \psi_1^i & \dots & \psi_{n_s}^i \end{bmatrix} [T_{\text{disp}}] \{x_p(t)\} \quad (3.59)$$

Given this load, the strain due to bending is determined using the following relation from Euler-Bernoulli linear beam theory:

$$\varepsilon_y = -\frac{M_x \cdot z}{I_{zz} \cdot E} \quad (3.60)$$

where ε_y is the strain, M_x is the bending moment (from the relevant DOF of $\{L\}$), z is the z -distance of the sensor from the elastic axis of the beam, I_{zz} is the z -axis area moment of inertia, and E is the modulus of elasticity. Although the axial load in the y -direction would also add to the strain output, its effect is negligible compared to that of bending. This is especially true because the axial y -stress at rest due to the weight of the model is tared out at before tests. Thus, its effect has been omitted in modeling.

The strain gauge on MARGE is mounted on the lower surface of the rectangular cross-sectioned wing spar. Thus, z is equal to negative one half of the spar thickness t :

$$\varepsilon_y = -\frac{M_x \cdot (-t/2)}{I_{zz} \cdot E} \quad (3.61)$$

Combining Eqs. 3.59 and 3.60 yields the final expression for MARGE's strain output, u_4 :

$$u_4 = \frac{t/2}{I_{zz} \cdot E} \begin{bmatrix} \psi_1^4 & \dots & \psi_{n_s}^4 \end{bmatrix} [T_{\text{disp}}] \{x_p(t)\} \quad (3.62)$$

Thus, the full expression for the plant output of MARGE is

$$\{y_p\} = \begin{bmatrix} [\phi^1] [T_{\text{vel}}][A_p] \\ [\phi^2] [T_{\text{vel}}][A_p] \\ [\phi^3] [T_{\text{vel}}][A_p] \\ \frac{t/2}{I_{zz} \cdot E} \begin{bmatrix} \psi_1^4 & \dots & \psi_{n_s}^4 \end{bmatrix} [T_{\text{disp}}] \\ [\phi^5] [T_{\text{disp}}] \\ [\phi^5] [T_{\text{vel}}] \end{bmatrix} \{x_p\} + \begin{bmatrix} [\phi^1] [T_{\text{vel}}][B_p] \\ [\phi^2] [T_{\text{vel}}][B_p] \\ [\phi^3] [T_{\text{vel}}][B_p] \\ 0 \\ 0 \\ 0 \end{bmatrix} \{u_p\} \quad (3.63)$$

Thus, the plant output of MARGE has been derived the form that is desired

$$\{y_p\} = [C_p]\{x_p\} + [D_p]\{u_p\} \quad (3.64)$$

where $[C_p]$ and $[D_p]$ are the block matrices in Eq. 3.63.

3.3 Actuation and Sensing Dynamics

When developing a model that is used for control design, the dynamics of the actuators and sensors must be accounted for. The output of the control law will be fed not into the plant, but the imperfect actuators. The input of the control law will come not directly from the plant, but from the imperfect sensors. Thus, the goal of this section is to determine dynamic models for the actuators and the sensors in the forms

$$\begin{aligned}\frac{d}{dt}\{x_{act}\} &= [A_{act}]\{x_{act}\} + [B_{act}]\{u_{act}\} \\ \{y_{act}\} &= [C_{act}]\{x_{act}\} + [D_{act}]\{u_{act}\}\end{aligned}\tag{3.65}$$

and

$$\begin{aligned}\frac{d}{dt}\{x_{sens}\} &= [A_{sens}]\{x_{sens}\} + [B_{sens}]\{u_{sens}\} \\ \{y_{sens}\} &= [C_{sens}]\{x_{sens}\} + [D_{sens}]\{u_{sens}\}\end{aligned}\tag{3.66}$$

3.3.1 Control Surfaces

The servo-actuated control surfaces on the wing and tail are known (from [5]) to have dynamics according to the following transfer function¹:

$$G(s) = \frac{1461}{s^2 + 62.2s + 1461}\tag{3.67}$$

This transfer function has the response shown in Figure 3.1.

¹The numerator of this transfer function differs from that defined in [5] because the actuator is calibrated to have unity DC gain before use.

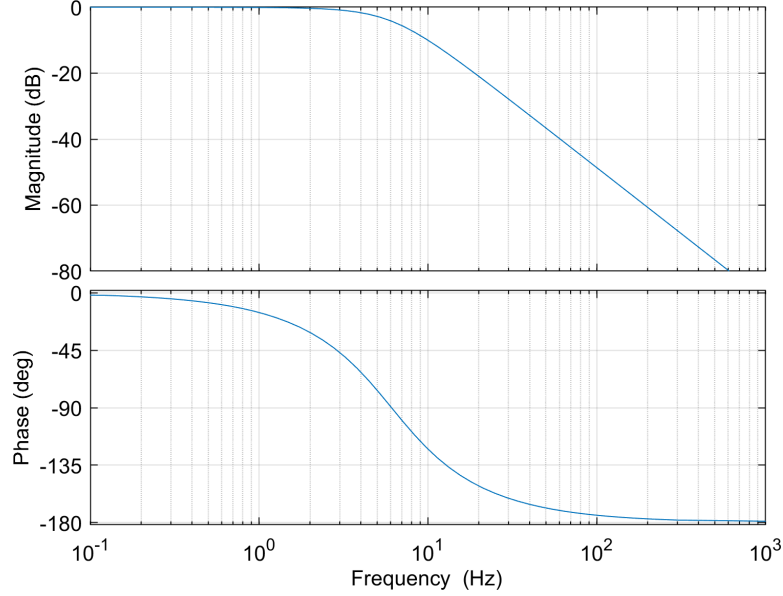


Figure 3.1: Bode plot of actuator transfer function

This transfer function was then converted to the following equivalent state-space representation:

$$\begin{aligned} s\{x\} &= \begin{bmatrix} -62.2 & -1461 \\ 1 & 0 \end{bmatrix} \{x\} + \begin{bmatrix} 0 \\ 1 \end{bmatrix} u \\ y &= \begin{bmatrix} 0 & 1461 \end{bmatrix} \{x\} \end{aligned} \quad (3.68)$$

where u is the input, y is the output, and $\{x\}$ is the internal state of the actuator.

3.3.2 Gust Vanes

The wind tunnel gust vanes were measured to have “perfect” dynamics except for a pure time delay of 0.34 seconds. This pure delay was approximated as a second-order transfer function using a Padé approximant:

$$G(s) = \frac{s^2 - 176.47s + 10381}{s^2 + 176.47s + 10381} \quad (3.69)$$

The Padé approximant matches the pure delay’s response well in the frequency range of interest (<20 Hz); the step response and phase shift behavior of a pure delay and the Padé

approximant are compared in Fig. 3.2.

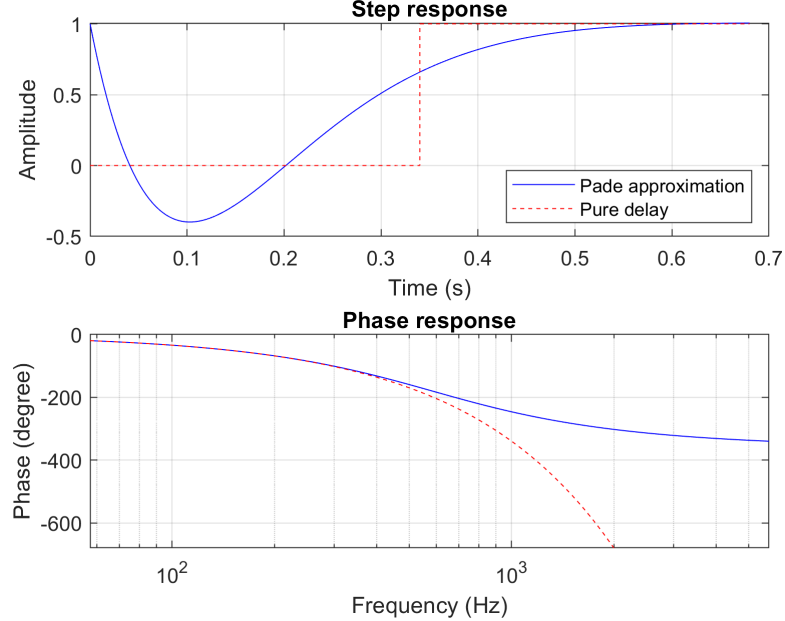


Figure 3.2: Padé approximant of the pure-delay response of the wind tunnel gust vanes

This transfer function was then converted to the following equivalent state-space representation:

$$\begin{aligned} s\{x\} &= \begin{bmatrix} -176.47 & -10381 \\ 1 & 0 \end{bmatrix} \{x\} + \begin{bmatrix} 1 \\ 0 \end{bmatrix} u \\ y &= \begin{bmatrix} -352.94 & 0 \end{bmatrix} \{x\} + \begin{bmatrix} 1 \end{bmatrix} u \end{aligned} \quad (3.70)$$

where u is the input, y is the output, and $\{x\}$ is the internal state of the actuator.

3.3.3 Combined Actuation and Sensing

The state-space models for the four actuators (three servo-actuated control surfaces and one pair of wind tunnel gust vanes) are combined to form one combined state-space model

for all actuators with input, output, and state

$$\{u_{\text{act}}\} = \begin{bmatrix} u_1 \\ u_2 \\ u_3 \\ u_4 \end{bmatrix} \quad \{y_{\text{act}}\} = \begin{bmatrix} y_1 \\ y_2 \\ y_3 \\ y_4 \end{bmatrix} \quad \{x_{\text{act}}\} = \begin{bmatrix} \{x\}_1 \\ \{x\}_2 \\ \{x\}_3 \\ \{x\}_4 \end{bmatrix} \quad (3.71)$$

respectively. The combined actuation state-space model is then

$$\begin{aligned} \{x_{\text{act}}\} &= \begin{bmatrix} [A_1] & & & \\ & [A_2] & & \\ & & [A_3] & \\ & & & [A_4] \end{bmatrix} \{x_{\text{act}}\} + \begin{bmatrix} [B_1] & & & \\ & [B_2] & & \\ & & [B_3] & \\ & & & [B_4] \end{bmatrix} \{u_{\text{act}}\} \\ \{y_{\text{act}}\} &= \begin{bmatrix} [C_1] & & & \\ & [C_2] & & \\ & & [C_3] & \\ & & & [C_4] \end{bmatrix} \{x_{\text{act}}\} + \begin{bmatrix} [D_1] & & & \\ & [D_2] & & \\ & & [D_3] & \\ & & & [D_4] \end{bmatrix} \{u_{\text{act}}\} \end{aligned} \quad (3.72)$$

where the $[A]$, $[B]$, $[C]$, and $[D]$ system matrices for the two types of actuators are defined above in Eq. 3.68 and 3.70. This then forms the actuator block shown in Fig. 3.3.

A similar process would be appropriate for a set of imperfect sensors. However, the high-rate sensors used in MARGE have approximately no dynamics in the frequency range of interest. Thus, the sensor response was approximated as

$$\{y_{\text{sens}}\} = [I]\{u_{\text{sens}}\} \quad (3.73)$$

In other words, the output of the sensor was taken as the output of the plant. This then forms the sensor block shown in Fig. 3.3.

3.4 Coupled Aeroservoelastic Modeling

The imperfect actuators and sensors can be accounted for in modeling by combining the actuator, plant, and sensor models into an integrated system model that can then be used

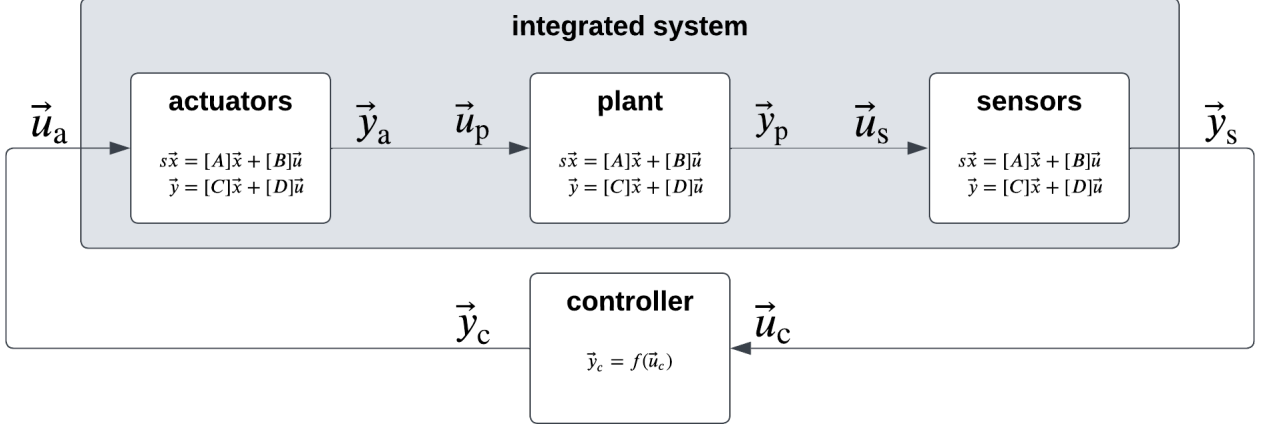


Figure 3.3: Integrated model of actuation, plant, and sensing in a control loop

for control design; see Fig. 3.3 for a block diagram of this system of systems. In the system illustration in Fig. 3.3, the actuators take in the control command and output control forces; the plant takes in control forces and outputs motions; the sensors take in motions and output measured motions; and a control law can then use this measured motion to create a control command for MARGE.

First, the actuator dynamics can be coupled to the plant dynamics. In state-space form, this is

$$s \begin{Bmatrix} \{x_{act}\} \\ \{x_p\} \end{Bmatrix} = \begin{bmatrix} [A_{act}] & [0] \\ [B_p][C_{act}] & [A_p] \end{bmatrix} \begin{Bmatrix} \{x_{act}\} \\ \{x_p\} \end{Bmatrix} + \begin{bmatrix} [B_{act}] \\ [B_p][D_{act}] \end{bmatrix} \{u_{act}\} \quad (3.74)$$

where the entries in the block matrices containing $[B_p]$ are used to convert $\{x_{act}\}$ and $\{u_{act}\}$ into the plant's input, $\{u_p\} = \{y_{act}\}$.

The actuator can similarly be coupled to the plant in the output equations:

$$\{y_p\} = \begin{bmatrix} [D_p][C_{act}] & [C_p] \end{bmatrix} \begin{Bmatrix} \{x_{act}\} \\ \{x_p\} \end{Bmatrix} + [D_p][D_{act}]\{u_{act}\} \quad (3.75)$$

where similarly, the terms involving $[D_p]$ are used to convert $\{x_{act}\}$ and $\{u_{act}\}$ into the plant's input, $\{u_p\} = \{y_{act}\}$.

The block matrices in Eq. 3.74 and 3.75 form the coupled actuator-plant system in Fig. 3.3. Since the sensors are modeled as perfect, this is also equivalent to the coupled actuator-plant-sensor system. Thus, Eq. 3.74 and 3.75 define the state-full, coupled space model for MARGE in the form required as defined in Eq. 3.1.

Chapter 4

FINITE ELEMENT MODELING

An existing finite element model (FEM) of MARGE was updated in this study using NASTRAN. The model included MARGE, the wind tunnel test section walls, and the gust vanes. This chapter describes the FEM; the updates applied to it are documented in Section 5.4.

The wing structure and tail structure were each modeled as a single chain of Euler-Bernoulli beam elements along their respective spar. The wind tunnel walls were modeled as extremely rigid panels whose contribution to the structural dynamics of the FEM is negligible. The area moments of inertia and material properties of the beam elements in the finite element model are reported in Table 4.1.

Table 4.1: Properties of Beam Finite Elements

	E , GPa	G , GPa	I_1 , mm ⁴	I_2 , mm ⁴	J , mm ⁴
wing spar	68.9	0.0125	25.41	58530	58560
tail spar	68.9	25.9	1829	13010	14840
fuselage	200	76.0	74.52	4476	4550
rigid	10^4	10^4	25.41	58530	58560

Note that the values in Table 4.1 (and also Table 4.2) are the final values after corrections. The values before corrections and correction process are discussed in Section 5.4.

The aerodynamic loads on the NASTRAN model are based on the doublet-lattice model (DLM) for aerodynamics. This linear aerodynamic model assumes incompressible, inviscid, irrotational flow around thin lifting surfaces. The loads on the aerodynamic panels were

transferred to the structural nodes via a spline interpolation. The aerodynamic panels and structural finite elements can be seen in Fig. 4.1. Figure 4.2 shows a close-up view of MARGE in the FEM. Details of the implementations and limitations of these theories can be found in the NASTRAN Aeroelastic Analysis User's Guide [9]

The structural dynamic solution to the FEM includes natural frequencies and mode shapes. These are summarized in Table 4.2.

Table 4.2: NASTRAN Modal Properties

#	ω_n	Description
1	0	pitching
2	1.444	wing bending 1
3	10.487	wing bending 2
4	16.638	fuselage bending 1
5	19.200	wing twisting 1
6	21.948	fuselage in-plane bending 1
7	32.311	wing bending 3
8	60.852	fuselage bending 2
9	66.011	wing bending 4
10	69.298	wing in-plane bending 1
11	113.674	wing bending 5
12	120.642	fuselage bending 3
13	153.716	fuselage in-plane bending 2
14	160.909	fuselage bending 4
15	175.941	wing bending 6

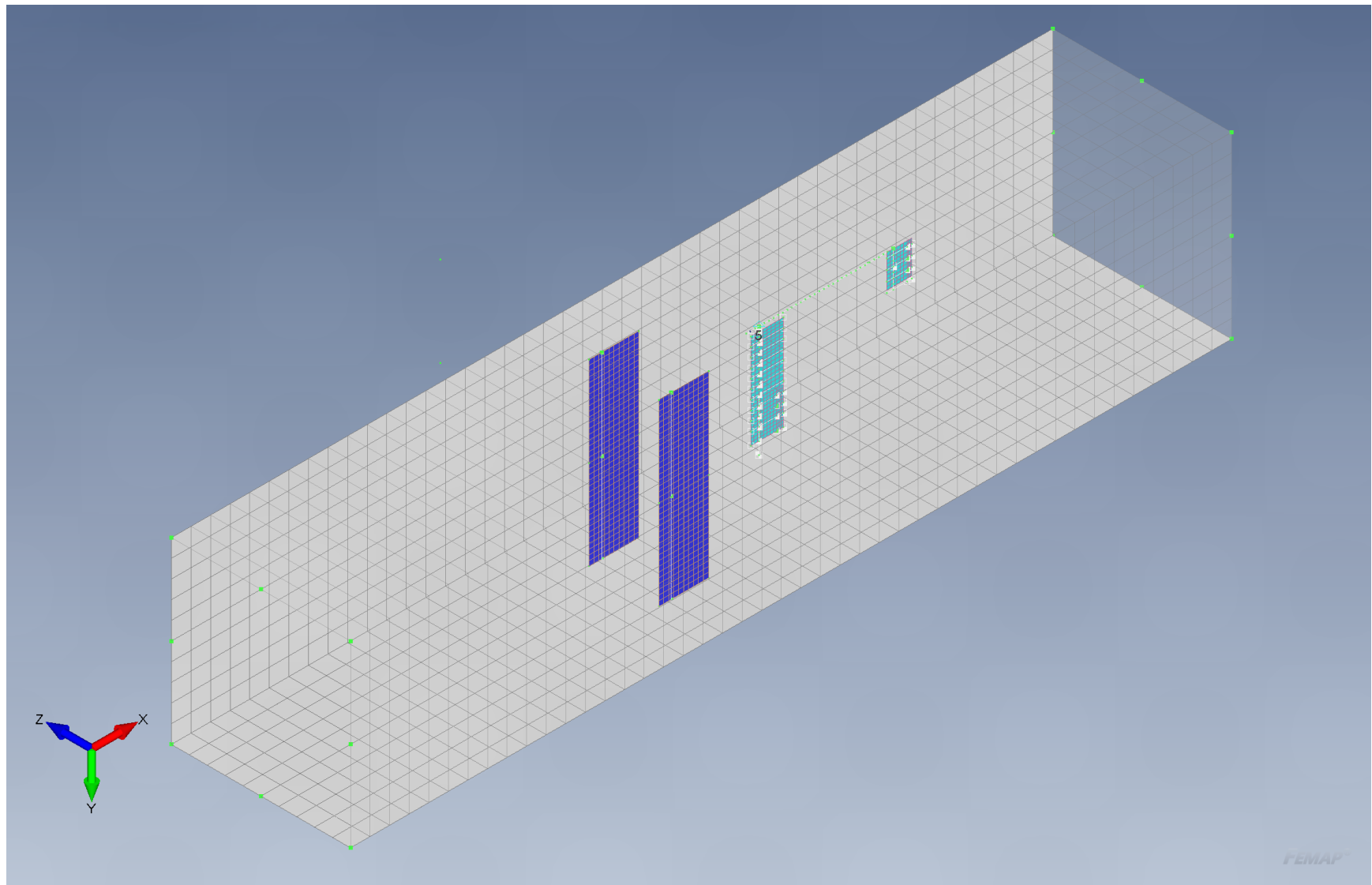


Figure 4.1: NASTRAN finite-element model of MARGE, gust vanes, and wind tunnel walls

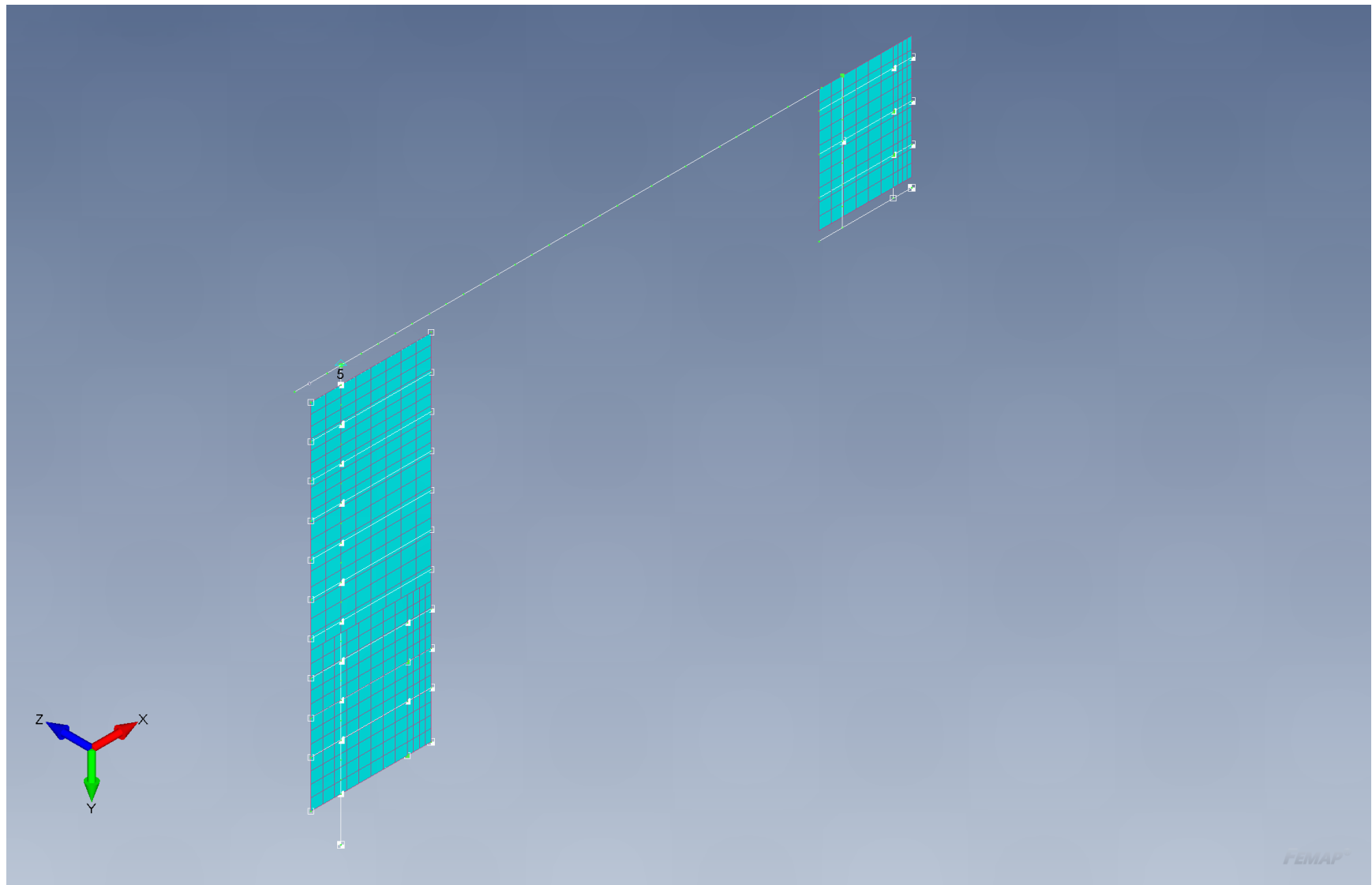


Figure 4.2: NASTRAN finite-element model, close-up of MARGE only

Chapter 5

GROUND VIBRATION TESTING

Ground vibration testing (GVT) was performed to validate the preliminary finite-element model of MARGE. The frequency responses of accelerometers to an impulse input were generated from the experimental data. Using these, the natural frequencies and the damping ratios of dynamic modes of the system were determined.

Two sets of data were collected. The first set of data was collected with MARGE as designed, including the rigid-body pitching mode. This data was used to determine the damping ratios of the modes. The second set of data was collected with the root of the MARGE wing clamped to eliminate the rotational rigid-body mode. This was done to enable data acquisition of flexible-body modes without exciting and losing energy to the rigid-body mode. This data was used to tune the finite-element model and to determine the damping ratios of the wing bending modes.

5.1 *Experiment*

This section describes the GVT setup and procedure.

5.1.1 *Test Setup*

The equipment used for the test include:

- PCB Piezotronics ICP Impact Hammer Model 086C03
- PCB Piezotronics ICP Accelerometer Model 352C22
- National Instruments DAQ Model NI-9234

The impact hammer and accelerometers were connected to the DAQ system which was connected to a personal computer via Ethernet. The computer interfaced with the DAQ system using the Data Acquisition Toolbox for MATLAB. Data was acquired at a rate of at least 6400 Hz.

The accelerometers were mounted in locations such that all of the flexible natural modes of interest were observable. This was done by placing accelerometers near anti-nodal points of the natural modes as predicted by the preliminary finite-element model. The accelerometer locations (and corresponding FEM node IDs) for the two sets of testing are shown in Fig. 5.1. The impact hammer hits were also placed at these same locations on the structure.

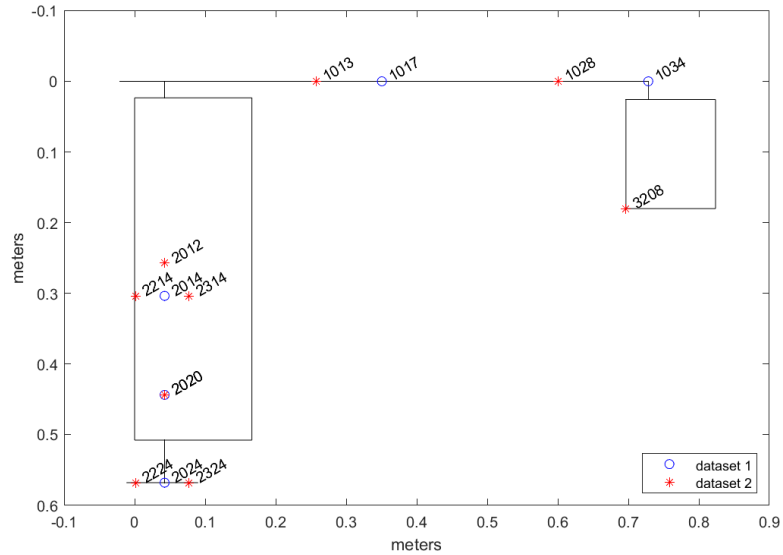


Figure 5.1: Accelerometer placement in ground vibration testing of MARGE

For the second dataset, pairs of accelerometers on the wing located a short distance apart chordwise were also treated as a fictional third accelerometer by taking the difference of their signals. This was done to simulate a sensor observing only torsional modes of the wing.

5.1.2 Test Procedure

Tests were performed by executing a MATLAB script which would prompt the user to name and record data. After data acquisition for a run the script automatically searched for the moment of impact generated a plot of the full time-series as well as a magnified plot of the time-series data around the impact. This magnified view was used to inspect for double-hits from the impact hammer. The script also automatically rejected data which was of insufficient length or which had too weak or strong of an impact from the hammer.

After accelerometers were mounted to MARGE and the DAQ was connected to the host computer, the following procedure was used for each run of GVT:

1. Start recording data
2. Hit the target point with the impact hammer
3. After at least five seconds has elapsed, stop recording data
4. Inspect the automatically-generated plot of the time-series data for irregularities, especially double-hits of the impact hammer or bumps of the accelerometers
5. Name and save the data

The result of this procedure is one run of time-series data such as that shown in Figure 5.2

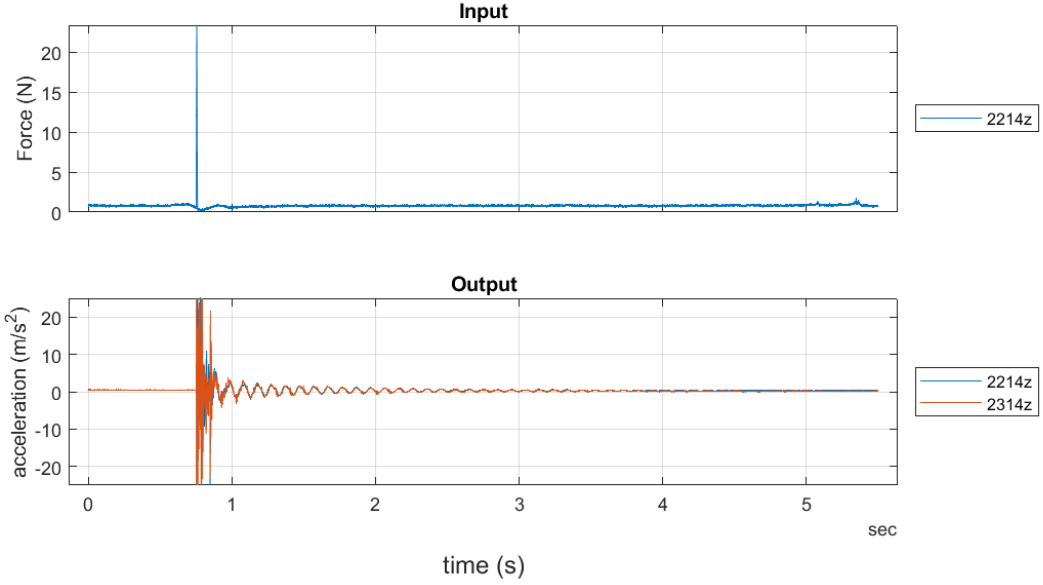


Figure 5.2: Example GVT time-series data from an impulse at the location 2214z

5.2 Generating Frequency Response Functions

Each GVT test point (input-output combination) was post-processed to generate the frequency response functions (FRFs) of the accelerometers to the impacts. This section describes the steps in this process.

5.2.1 Time-Domain Post-Processing

The time-series data was truncated to start just before the impulse input and end after t seconds where t was chosen to be at least four times the period of the lowest frequency of interest. (In most cases, $t = 4$ seconds.) This ensured that irrelevant segments of the signal were eliminated while keeping still enough data to perform the frequency-domain analysis.

Each test point was recorded as three (in the second dataset) or five (in the first dataset) separate impacts. After truncation, the signals from these impacts were concatenated to form one continuous time-domain signal. The mean of this combined signal was then subtracted

from it so that there would be no steady-state component before proceeding to compute the frequency response.

5.2.2 Computing Frequency Response Functions

The frequency response functions for each of these concatenated SISO signal pairs were computed using the method described in [11]. This section summarizes this method as it was implemented for the GVT data.

First, the signal was buffered into overlapping Hann windows and transformed using a chirp z-transform (CZT). The CZT has an advantage over the similar Discrete Fourier Transform (DFT) in that it has the ability to allocate the full frequency-domain resolution to the bandwidth of interest. The purpose of first buffering the signal is to reduce the effect of noise at the expense of frequency resolution.

The products of the CZT are the power spectra of the signals. For any given accelerometer power spectrum $S_y(\omega)$ and impact hammer power spectrum $S_x(\omega)$, the cross-spectrum correlation estimates can be computed as

$$G_{xy}(\omega) = S_x^* \cdot S_y(\omega) \quad (5.1)$$

$$G_{yx}(\omega) = S_y^* \cdot S_x(\omega) \quad (5.2)$$

and the autospectrum correlation estimates can be computed as

$$G_{xx}(\omega) = |S_x|^2 \quad (5.3)$$

$$G_{yy}(\omega) = |S_y|^2 \quad (5.4)$$

Three possible ways to estimate the FRF from the above are the H_1 FRF, the H_2 FRF, and the H_v FRF:

$$FRF_{H_1}(\omega) = \frac{G_{xy}(\omega)}{G_{xx}(\omega)} \quad (5.5)$$

$$FRF_{H_2}(\omega) = \frac{G_{yy}(\omega)}{G_{yx}(\omega)} \quad (5.6)$$

$$FRF_{H_v}(\omega) = \sqrt{FRF_{H_1}(\omega) \cdot FRF_{H_2}(\omega)} \quad (5.7)$$

The H_1 estimate tends to under-estimate the FRF when there is noise in the input, while the H_2 estimate tends to over-estimate the FRF when there is noise at the output [11]. The H_v estimate of the FRF is thus used in this study as a conservative choice which makes no assumption of the source or nature of noise in the system. (Subsequent references to the FRF can be assumed to refer to the H_v FRF.)

The coherence can also be computed as

$$\text{coh}(\omega) = \frac{|G_{xy}|^2}{|G_{xx}||G_{yy}|} \quad (5.8)$$

The result of this procedure is a frequency response such as that shown in Figure 5.3

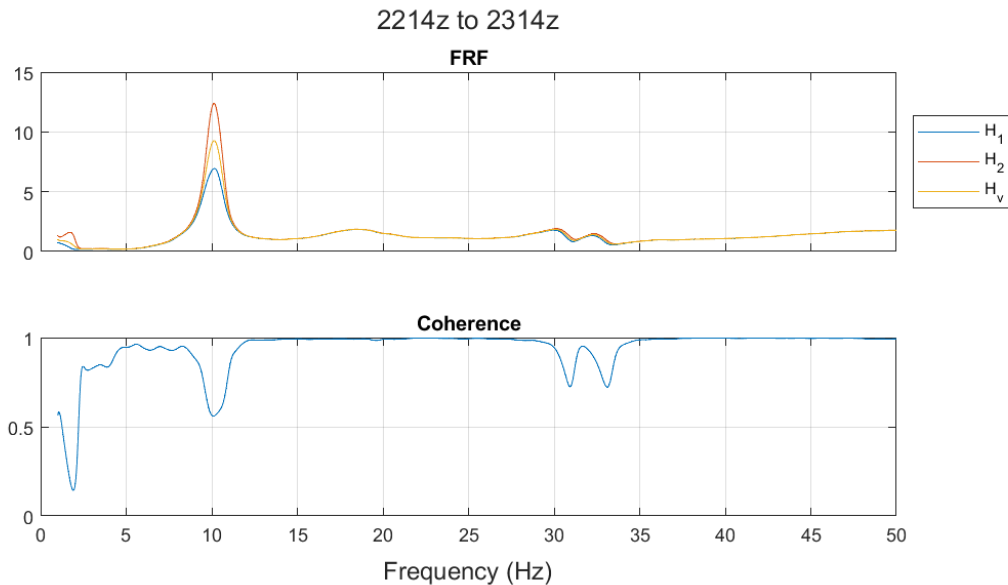


Figure 5.3: Example GVT frequency response data from an impulse at the location 2214z to an accelerometer at the location 2314z

The frequency response functions and coherence computed for the GVT data are shown in Appendix A.

5.3 Determining Modal Properties

Once the FRFs were obtained, the frequencies and damping ratios of the natural modes were computed from the FRFs. This section describes this computation.

5.3.1 Computing Natural Frequencies

First, natural frequencies visible as peaks in the data were noted. These often were visible across multiple FRFs, confirming that they were not artifacts from the noise of a single experimental trial.

These experimental natural frequencies were compared to those predicted by the NASTRAN finite-element model; if they matched well, it was assumed that the experimental natural frequency corresponded to the mode shape generated by the NASTRAN model. This could be further validated by observing the antinodal points of the relevant NASTRAN mode shape and checking that the FRFs in which the natural frequency peaks are visible correspond to sensors placed near those antinodal points.

In some cases, there were clear natural modes visible in the experimental data that were not predicted by the NASTRAN finite-element model. It was inferred that two of these natural modes appeared in that these were torsional modes of the wing, because the FRFs they appeared most prominently in were from the aforementioned “fictional” accelerometers which had manipulated signals to enhance the response to torsional modes. These torsional modes were not predicted by the preliminary NASTRAN finite-element model; this was corrected in the subsequent FEM tuning process.

Each experimental natural frequency ω_n was then measured in an automated way: first, all FRFs with a local maximum magnitude at ω_n which was at least twice the magnitude of its surroundings was identified. The median of all of these measured natural frequencies, each from a different FRF, was then taken to be the true experimental natural frequency for that natural mode.

5.3.2 Computing Damping Ratios

The damping ratio was also measured in a similar automated way. The damping ratio was computed for each identifiable natural frequency in each FRF using the half-power method:

$$\zeta = \frac{\omega_2 - \omega_1}{2\omega_n} \quad (5.9)$$

where

$$FRF(\omega_1) = FRF(\omega_2) = \frac{1}{2}FRF(\omega_n) \quad (5.10)$$

$$\omega_1 < \omega_2$$

The median of all of these damping ratios, each from a different FRF, was then taken to be the true damping ratio for that natural mode. The experimentally obtained natural frequencies and corresponding damping ratios can be found in Table 5.2.

5.4 Finite Element Model Correction

The finite-element model was adjusted to better match the experimental GVT data as well as static testing data from a separate study. This was done by adjusting the bending and torsional stiffness of the various materials until the natural frequencies best matched that of the experiment; the values of these before and after correction are shown in Table 5.1. The uncorrected and corrected natural frequencies of the FEM are compared to the experimental natural frequencies in Fig. 5.4. Note that damping ratios are not involved here, as the FEM does not model damping. The damping ratios are used only in the modeling in Chapter 3.

Table 5.1: Finite-Element Model Material Parameter Adjustment

component	old E (Pa)	old G (Pa)	new E (Pa)	new G (Pa)
fuselage	2.00×10^{11}	7.58×10^{10}	1.80×10^{11}	7.60×10^{10}
wing spar	6.89×10^{10}	2.59×10^{10}	6.89×10^{10}	1.25×10^7
tail spar	6.89×10^{10}	2.59×10^{10}	6.89×10^{10}	2.59×10^7

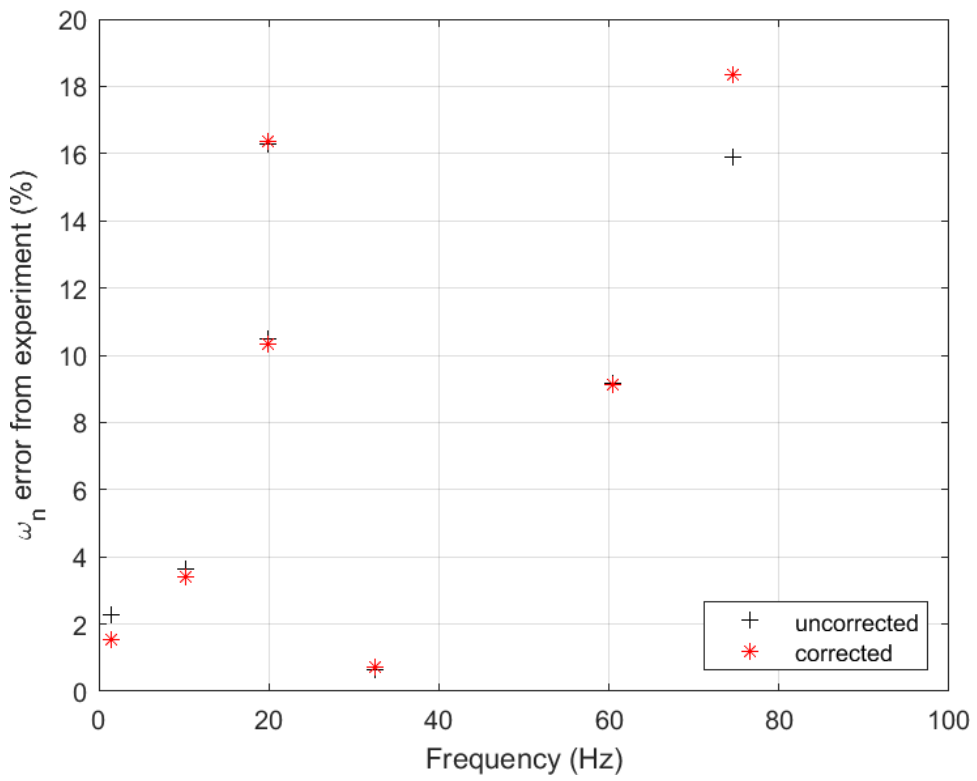


Figure 5.4: Finite-element model material parameter adjustment

Table 5.2: Natural Frequencies of Uncorrected FEM, Corrected FEM, and Experiment

Uncorrected FEM (Hz)	Corrected FEM (Hz)	Experiment (Hz)	Description
0	0		pitching
1.454401	1.44397	1.422	wing bending 1
10.51099	10.48667	10.142	wing bending 2
-	19.1997	18.094	wing twisting 1
23.13519	21.94804	19.893	fuselage in-plane bending 1
17.81394	16.63828	19.897	fuselage bending 1
32.33148	32.31077	32.545	wing bending 3
-	-	51.706	wing twisting 2
66.02579	66.01089	60.482	wing bending 4
69.7988	69.29826		wing in-plane bending 1
62.68383	60.85218	74.521	fuselage bending 2
113.6852	113.6736		wing bending 5
120.8188	120.6415		fuselage bending 3
161.7024	153.716		fuselage in-plane bending 2
175.9587	175.9407		wing bending 6
159.36	160.9085		fuselage bending 4
225.7709	-		fuselage bending 5

Chapter 6

WIND TUNNEL TESTING

This chapter describes the wind-tunnel testing of MARGE and the post-processing of the wind tunnel test data.

MARGE was tested at the University of Washington's 3x3 low-speed wind tunnel at six flight conditions, $q_D = \{60, 100, 163, 207, 281, 343\}$ Pa. At each flight condition, the response to each of the four inputs was tested three times. For the gust vanes, a discrete 4-degree doublet gust was generated with a frequency of 1.45 Hz (approximately equivalent to the first wing bending natural frequency). For the ailerons, a 5-degree frequency sweep from 1 Hz to 2 Hz was performed. For the elevator, a 2-degree frequency sweep from 1 Hz to 2 Hz was performed. The sweep's frequency band was chosen to encompass the first wing bending mode while staying within the bandwidth of the actuators.

The exception to the above is at $q_D = 343$ Pa. At this dynamic pressure, the aileron sweeps were reduced in magnitude to 3.5 degrees and the elevator sweep was reduced in magnitude to 1 degree. This was done in order to reduce the risk of damage to the model due to violent responses at high speeds.

All of these tests were controlled and recorded using Simulink Real-Time. The testing yielded time-series data of input commands and sensor readings for each test. An example of a single run of data is shown in Fig. 6.1

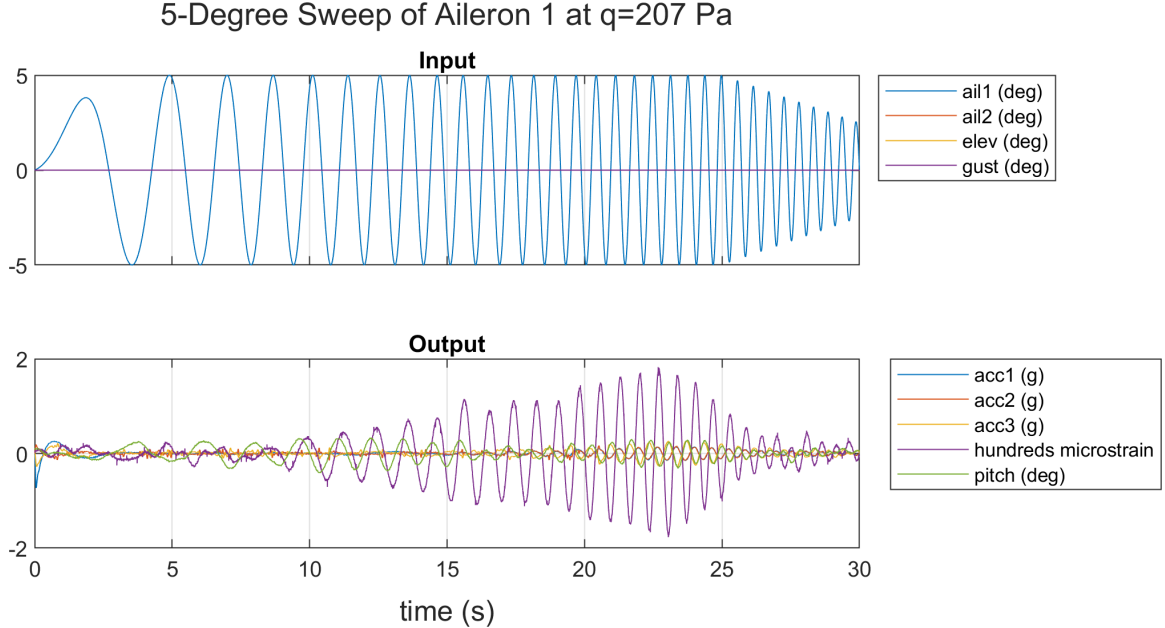


Figure 6.1: Sample wind tunnel time-series data from a single run

6.1 Data Postprocessing

The time-domain data was post-processed in a similar way as was done for the GVT data in Section 5.2. Each run's data was truncated to start when the input began and end five seconds after the input ended. The data was re-centered to have zero mean and then the three runs of each test were concatenated.

This single concatenated time-domain signal was then buffered into overlapping Hann windows and transformed using the CZT. The FRFs were then computing using Equation 5.7. The FRFs were computed from 0.4 Hz to 2.0 Hz.

6.1.1 Accelerometer Data Postprocessing

The output of the accelerometers contained significant noise and potentially contained electrical interference from other components in MARGE. Thus, the uncertainty in FRFs between inputs and the accelerometers was high. This was compensated for by specifically

filtering the time-series signal from accelerometers before other postprocessing and limiting the bandwidth of the FRFs produced to within a range in which the accelerometers tend to behave more consistently.

Before going through the postprocessing steps outlined above, the time-series signal from the accelerometers was filtered using a Butterworth bandpass filter which limited frequencies in the signal to between 0.8 Hz and 25 Hz. This was done to reduce the effect of both high-frequency noise and low-frequency drift in the acclerometer signals. This same bandpass filter was applied to the input signal when generating FRFs between an input and the accelerometers so that the filter would not skew the FRF.

Unlike for other input-output combinations, all FRFs of an input to an accelerometer were only computed between 1 Hz and 2 Hz in the frequency domain. This was because the H_1 and H_2 FRFs diverged significantly outside of these bounds, indicating high uncertainty in the FRFs due to issues in the data (such as noise).

Chapter 7

MODEL TUNING AND RESULTS

The state-space model generated in Chapter 3 was adjusted such that its frequency response fit the experimental frequency response. This was done by adjusting certain parameters in the model that each represented some uncertainty in the model's physical characteristics. This adjustment was first done by hand, and then repeated in a automated process through optimization.

For this chapter, unless otherwise indicated, the state-space model was generated using $n_s = 2$ structural dynamic modes and $n_{\text{lag}} = 0$ lag terms in the Roger Approximation. This was done in order to obtain a low-order model which still could accurately capture the dynamics at low frequencies, such as those in the bandwidth of the actuators.

7.1 Tuning Parameters

The state-space model derived in Chapter 3 assumes linear structural dynamics, linear aerodynamics, and thin airfoils. It also requires perfect knowledge of mode shapes. In reality, MARGE does not conform to any of these assumptions perfectly. Thus, tuning parameters were implemented in the state-space model generation script which adjusted the structural and aerodynamic modeling to compensate for these nonlinearities and inaccuracies.

The first tuning parameter is the first wing bending natural frequency ω_{n2} . This quantity has a low uncertainty, but was treated as a tuning parameter for purposes of investigation.

The next tuning parameters are the damping ratios ζ for the modes. These have higher uncertainty since viscous damping is not the most physically accurate model for structural damping. Furthermore, aerodynamic damping of motions is not accounted for in the model. These can be compensated for by adjusting the damping ratios of the modes to capture all

the mechanisms of damping in one place.

The next tuning parameters are the effectiveness τ of the controls. Each control surface will not be as effective as predicted by the linear aerodynamic model due to airfoil thickness, viscous effects (such as flow separation), roughness, and gaps in construction. These can be compensated for by adjusting the control effectiveness of each control surface. These tuning parameters scale the forces predicted for the control surfaces by the linear aerodynamic model.

The final tuning parameters are scaling factors $\tau_{P_{ss}}$ for each entry of $[P_{ss}]$. (Refer to Eq. 3.18 for the context in which $[P_{ss}]$ is used in modeling.) These scale the lift of the lifting surfaces (not including the control surfaces) to account for airfoil thickness, viscous effects, roughness, and gaps in construction.

A summary of tuning parameters and their default values (corresponding to no corrections) is shown in Table 7.1. The comparison of this initial un-tuned model's FRFs and the experimental FRFs can be seen in Fig. 7.1.

Note that Table 7.1 applies for the case of $n_s = 2$ structural dynamic modes used in modeling. When a higher number of modes is used, $\{\zeta\}$ continues to extend with damping ratios of higher modes from the GVT results (found in Table 5.2) and the Roger matrix scaling factors $[\tau_{P_{ssi}}]$ are a larger matrix of ones.

Table 7.1: Default Values of MARGE Tuning Parameters

Name	Default Value	Description
$\omega_{n,2}$	1.4544	first wing bending mode frequency
$\{\zeta\}$	$\begin{cases} 0 \\ 0.028 \end{cases}$	modal damping ratios
τ_{ail1}	1	aileron 1 effectiveness scaling
τ_{ail2}	1	aileron 2 effectiveness scaling
τ_{elev}	1	elevator effectiveness scaling
τ_{gust}	1	gust vane effectiveness scaling
$[\tau_{P_{ss1}}]$	$\begin{bmatrix} 1 & 1 \\ 1 & 1 \end{bmatrix}$	scaling lift from state
$[\tau_{P_{ss2}}]$	$\begin{bmatrix} 1 & 1 \\ 1 & 1 \end{bmatrix}$	scaling lift from state rates
$[\tau_{P_{ss3}}]$	$\begin{bmatrix} 1 & 1 \\ 1 & 1 \end{bmatrix}$	scaling lift from state accelerations

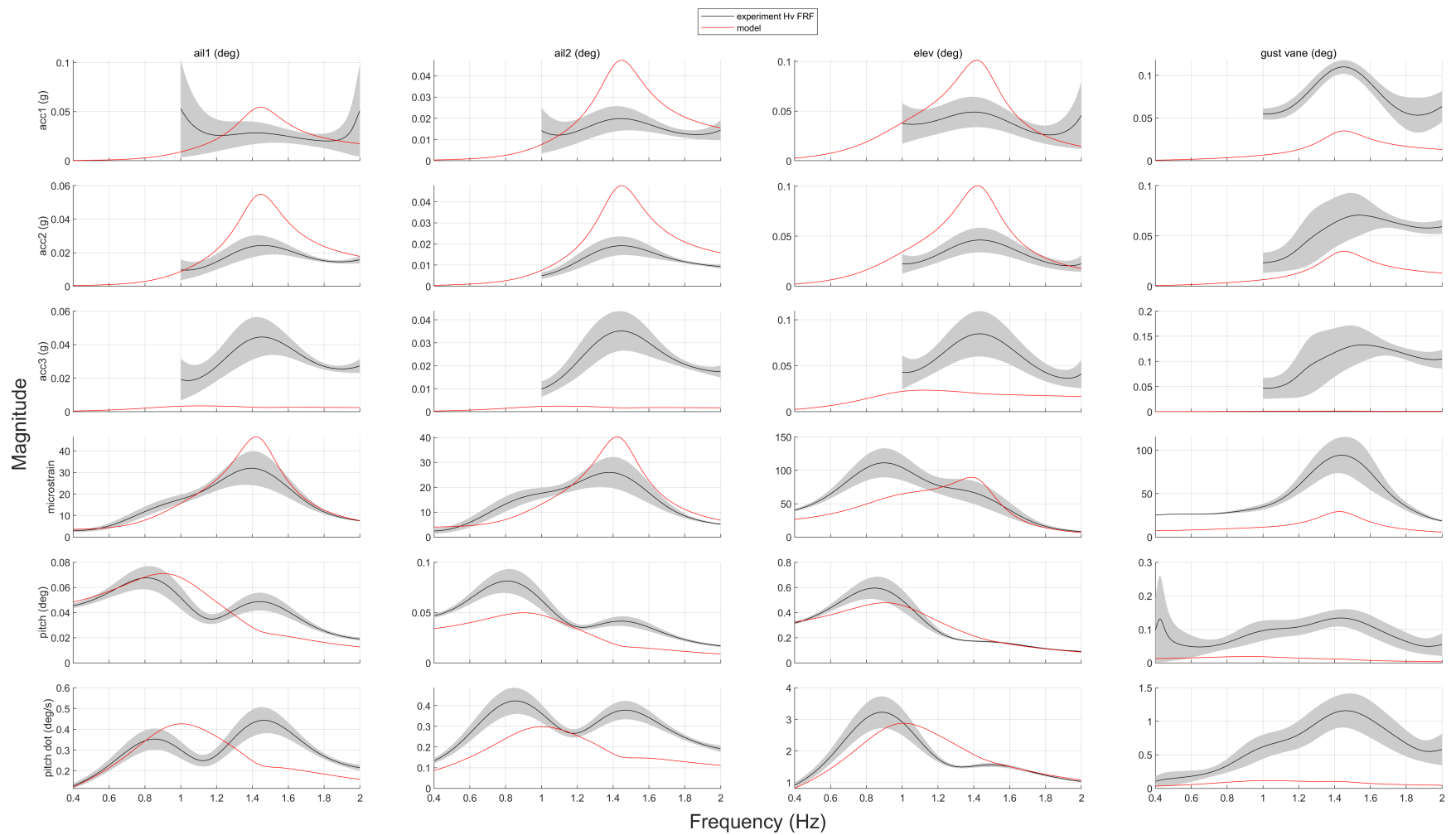


Figure 7.1: A comparison of experimental FRFs and untuned model FRFs at $q = 207$ Pa. The grey region is enclosed by the experimental H_1 FRF below and the experimental H_2 FRF above.

7.2 Manual Model Tuning

The first step in tuning the model was experimenting with manually tuning the parameters with the goal of closing the gap between the model's FRF and the experimental FRF at a single airspeed ($q_D = 207$). This was done by thinking intuitively about the modeling uncertainties which are most likely effecting the known discrepancies in the FRFs. For example, it was known that linear aerodynamics would overpredict the control surface effectiveness by up to 50% even in reasonably small ($< 10^\circ$) deflections [12, 6]. Thus, the control effectiveness of the ailerons and elevator were lowered until the FRFs with these controls as inputs better matched the experimental FRFs in magnitude.

The resultant parameters and FRF comparison of the manually tuned model are shown below in Table 7.2 and Fig. 7.2. The poor alignment between the model and experiment in Fig 7.2 indicates that the simple and “intuitive” manual tuning is not sufficient to completely match the experiment.

Table 7.2: Manually Tuned Values of MARGE Tuning Parameters

Name	Default Value	Adjusted Value
$\omega_{n,2}$	1.4544	1.4544
ζ_1	0	60
ζ_2	0.028	0.028
τ_{ail1}	1	0.6
τ_{ail2}	1	0.7
τ_{elev}	1	0.6
τ_{gust}	1	1
$[\tau_{P_{ss1}}]$	$\begin{bmatrix} 1 & 1 \\ 1 & 1 \end{bmatrix}$	$\begin{bmatrix} 0.9 & 1 \\ 0.5 & 1.5 \end{bmatrix}$
$[\tau_{P_{ss2}}]$	$\begin{bmatrix} 1 & 1 \\ 1 & 1 \end{bmatrix}$	$\begin{bmatrix} 0.9 & 1 \\ 0.5 & 1.5 \end{bmatrix}$
$[\tau_{P_{ss3}}]$	$\begin{bmatrix} 1 & 1 \\ 1 & 1 \end{bmatrix}$	$\begin{bmatrix} 0.9 & 1 \\ 0.5 & 1.5 \end{bmatrix}$

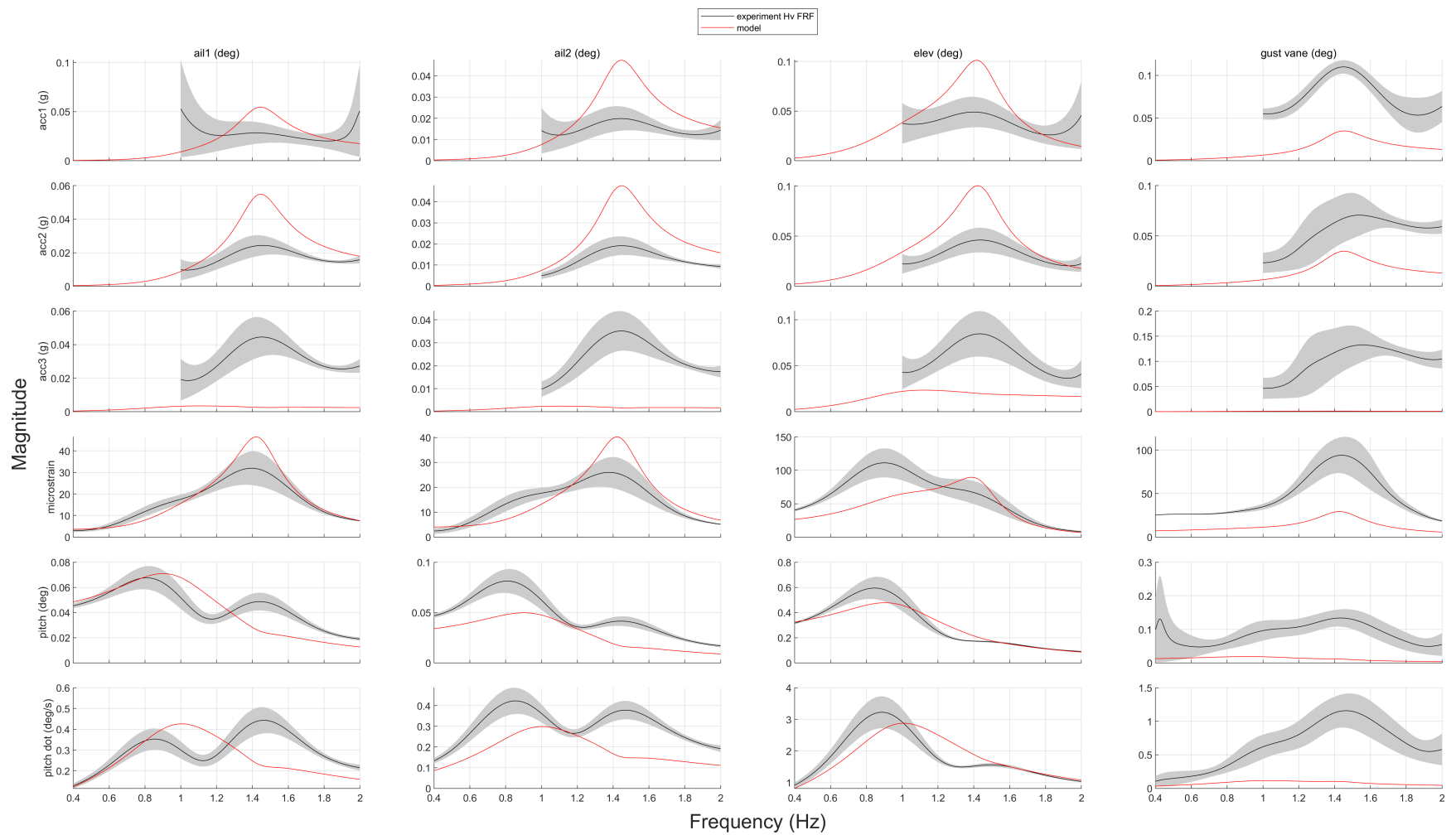


Figure 7.2: A comparison of experimental FRFs and manually-tuned model FRFs. The grey region is enclosed by the experimental H_1 FRF below and the experimental H_2 FRF above.

7.3 Model Optimization

The next step in tuning of MARGE’s state-space model was to tune using optimization. Using MATLAB’s `fmincon` function, gradient-based optimization was used minimize the error between the model’s FRFs and the experimental FRFs at all airspeeds by adjusting the tuning parameter design variables $\{x\}$ which contains the parameters listed in Table 7.1. In order to do this, an objective function was written which would perform the following computations:

1. generate MARGE’s state-space model
2. compute FRFs of the state-space model
3. compute a scalar measure of the difference between the model’s FRFs and the experimental FRFs

The first two computations were discussed in Chapter 3 and Section 6.

One additional difference between the automated tuning here and the manual tuning method presented in Section 7.2 is that the FRFs involving the accelerometers were ignored in this section. This was because, due to the issues mentioned in Section 6.1.1, the results from the accelerometers were too unreliable to use as a ground-truth for for error calculation.

7.3.1 Computing FRF Error

The third computation, the scalar measure of difference between FRFs, is performed as follows: First, the “error” in the magnitudes of the FRFs ϵ_{mag} and the “error” in the phase of the FRFs ϵ_{phase} are computed and summed across several frequencies in Eq. 7.1 and 7.2 respectively. Each difference in magnitude is normalized by the experimental magnitude at that frequency. The differences in phase are not normalized since they are already non-

dimensional (in radians).

$$\epsilon_{ij \text{ mag}}(\{x\}) = \sum_{\omega} \frac{|FRF_{\text{exp}}(\omega)| - |FRF_{\text{model}}(\{x\}, \omega)|}{|FRF_{\text{exp}}(\omega)|} \quad (7.1)$$

$$\epsilon_{ij \text{ phase}}(\{x\}) = \sum_{\omega} (\angle FRF_{\text{exp}}(\omega) - \angle FRF_{\text{model}}(\{x\}, \omega)) \quad (7.2)$$

The magnitude and phase errors are then combined in a weighted sum to create the total error f for an FRF. The weight λ determines whether the error magnitude or the error in phase is more important in the optimization. This weight is set by the user.

$$f_{ij}(\{x\}) = \epsilon_{ij \text{ mag}}(\{x\})\sqrt{\lambda} + \epsilon_{ij \text{ phase}}(\{x\})\frac{1}{\sqrt{\lambda}} \quad (7.3)$$

Finally the errors f for each FRF (corresponding to input-output pairs) are summed to create a total error F for MARGE. This is the objective function that the optimization algorithm minimizes.

$$F(\{x\}) = \sum_{i=1}^{N_{\text{in}}} \sum_{j=1}^{N_{\text{out}}} f_{ij}(\{x\}) \quad (7.4)$$

7.3.2 Design Variable Bounds

The tuning parameter design variables must be optimized within a bounded domain in order to guarantee a finite and physical solution. Thus, lower and upper bounds were placed on the design variables based on physical constraints and the level of expected uncertainty in the initial value. The bounds set on the design variables are listed in Table 7.3.

Note that all damping ratios are constrained to be positive. Also, all of the aerodynamic multipliers are bounded between zero and one. This is because linear aerodynamics is expected to overpredict forces, and thus a multiplier less than one is expected.

Table 7.3: Bounds of MARGE Tuning Parameter Design Variables

Name	Lower Bound	Upper Bound
$\omega_{n,2}$	0.9×1.4544	1.1×1.4544
ζ_1	0	∞
ζ_2	0.5×0.028	2×0.028
τ_{ail1}	0	1
τ_{ail2}	0	1
τ_{elev}	0	1
τ_{gust}	0	1
$[\tau_{P_{ss1}}]$	$\begin{bmatrix} 0 & 0 \\ 0 & 0 \end{bmatrix}$	$\begin{bmatrix} \infty & \infty \\ \infty & \infty \end{bmatrix}$
$[\tau_{P_{ss2}}]$	$\begin{bmatrix} 0 & 0 \\ 0 & 0 \end{bmatrix}$	$\begin{bmatrix} \infty & \infty \\ \infty & \infty \end{bmatrix}$
$[\tau_{P_{ss3}}]$	$\begin{bmatrix} 0 & 0 \\ 0 & 0 \end{bmatrix}$	$\begin{bmatrix} \infty & \infty \\ \infty & \infty \end{bmatrix}$

7.3.3 Optimization Results

A summary of the model properties, tuned parameters, and objective function values of several model tuning optimization studies are shown in Table 7.4. Each row of the table describes the parameters and the result of an optimization study. Select optimized tuning parameters corresponding to Table 7.4 can be found in Table 7.5.

Table 7.5: Select Model Tuning Optimized Parameters

#	$\omega_{n,2}$	ζ_1	ζ_2	τ_{ail1}	τ_{ail2}	τ_{elev}	τ_{gust}	$[\tau_{P_{ss1}}]$	$[\tau_{P_{ss2}}]$	$[\tau_{P_{ss3}}]$
1	1.58	5.96	0.0147	1.00	0.937	0.51	1.00	$\begin{bmatrix} 1.19 & 93.9 \\ 2.56 & 0.132 \\ 1.01 & 1.00 \\ 0.00277 & 1.50 \end{bmatrix}$	$\begin{bmatrix} 2.73 & 6.11 \\ 0.594 & 1.93 \\ 1.40 & 1.02 \\ 1.58 & 2.75 \end{bmatrix}$	$\begin{bmatrix} 0.0223 & 19.6 \\ 15.2 & 22.1 \\ 0.914 & 1.00 \\ 0.505 & 1.51 \end{bmatrix}$
4	1.46	60.0	0.028	0.497	0.452	0.547	0.652	$\begin{bmatrix} 1.05 & -145 \\ 2.71 & 17.4 \\ 0.410 & 6.71 \\ -0.351 & 1.22 \end{bmatrix}$	$\begin{bmatrix} 2.7 & 0.0893 \\ -0.0271 & 5.21 \\ 2.36 & -4.30 \\ -14.6 & 5.26 \end{bmatrix}$	$\begin{bmatrix} 63.1 & -199 \\ -8.38 & 48.6 \\ 1.11 & 0.968 \\ 1.63 & 1.03 \end{bmatrix}$
7	3.19	14.6	-0.0421	0.967	0.908	0.668	5.24	$\begin{bmatrix} 0.985 & -100.69 \\ 2.68 & 5.71 \\ 0.937 & 9.33 \\ 0.784 & 0.688 \end{bmatrix}$	$\begin{bmatrix} 1.85 & 19.9 \\ 10.5 & 2.00 \\ 3.87 & 4.34 \\ -5.30 & -1.59 \end{bmatrix}$	$\begin{bmatrix} 37.2 & -95.8 \\ -6.32 & 46.3 \\ 1.02 & 0.988 \\ 1.52 & 1.02 \end{bmatrix}$
10	-2.12	60.2	4.64	-3.37	-6.23	-6.30	0.447			
13	2.51	34.2	0.103	0.922	0.895	0.592	4.96			
16	3.49	60.2	8.27	-7.63	-2.68	-8.63	0.681			

Table 7.4: Model Tuning Optimization Results

#	n_s	n_{lag}	$\bar{\beta}_1$	$\bar{\beta}_2$	λ	$\{x_0\}$	bounds	$\epsilon_{\text{mag}}(\{x\})$	$\epsilon_{\text{phase}}(\{x\})$	$F(\{x\})$
1	2	0			1	default value	yes	328	447	775
2	2	0			1000	default value	yes	282	519	8947
3	2	0			0.001	default value	yes	355	438	1386
4	2	0			1	manual tune	yes	324	451	775
5	2	0			1000	manual tune	yes	282	519	8947
6	2	0			0.001	manual tune	yes	358	416	1317
7	2	0			1	manual tune	no	200	443	644
8	2	0			1000	manual tune	no	100	1354	3209
9	2	0			0.001	manual tune	no	727	419	1326
10	5	0			1	manual tune	no	164	417	581
11	5	0			1000	manual tune	no	124	1899	3986
12	5	0			0.001	manual tune	no	453	462	1463
13	2	2	0.2267	0.9067	1	manual tune	no	144	414	559
14	2	2	0.2267	0.9067	1000	manual tune	no	104	1622	3332
15	2	2	0.2267	0.9067	0.001	manual tune	no	230	371	1173
16	5	2	0.2267	0.9067	1	manual tune	no	227	486	713
17	5	2	0.2267	0.9067	1000	manual tune	no	176	912	5607
18	5	2	0.2267	0.9067	0.001	manual tune	no	347	408	1292

In general, as the model increases in size and constraints are loosened, the model optimization is capable of achieving a better result. One notable exception is the difference between the 13th and 16th optimization run. In Table 7.4, it can be seen that the increase from $n_s = 2$ to $n_s = 5$. Although the 16th run encodes more detailed dynamics with its five mode shapes, the inaccuracy of the mode shapes of the higher-frequency modes may have decreased this model's accuracy.

Optimization runs 3 and 6 differ only in their initial conditions. However, the runs reach different solutions, with one achieving a lower objective function than the other. This indicates that the objective function may have local minima which prevent the gradient-based optimization algorithm from reaching the true optimal solution.

Note that the optimized objective function values $F(\{x\})$ from Table 7.4 cannot be compared between runs with different weights λ (as their objective functions are different). However, the optimized magnitude and phase components $\epsilon_{\text{mag}}(\{x\})$ and $\epsilon_{\text{phase}}(\{x\})$ of the objective can be compared. In some cases, runs which only differ in λ differ greatly in these optimized components. This indicates that there can be a significant trade-off between achieving a good fit in the magnitude response and a good fit in the phase response.

As for the optimized parameters in 7.5, it can be seen that as soon as the physics-based bounds are removed (beginning in optimization run 7), the optimal tuning parameters immediately begin to take non-physical values. For example, the 10th optimization run resulted in a negative natural frequency $\omega_{n,2}$.

Notably, the 13th optimization run achieved the best result while also maintaining nearly all physically feasible tuning parameters. The only non-physical tuning outcome in this run is the first mode (rigid pitching) damping ratio. This, however, is not unexpected since the damping mechanisms present in reality are not perfectly captured by the linear viscous damping model utilized here. Otherwise, this is a physically realistic model which has been tuned to emulate the experimental data much more accurately than both the untuned model and the manually tuned model.

Thus, this model achieves the stated objective of this study: to obtain a accurate, physics-

based mathematical model for MARGE. The state-space matrices for this model can be found in Appendix B.

Chapter 8

CONCLUSION

This thesis has demonstrated a method for synthesizing a physics-based mathematical model for MARGE. Data from ground vibration testing was obtained which was used to improve the accuracy of the finite-element model. The finite element model was then the basis for the mathematical model, and physics-based tuning parameters were applied which increased its accuracy significantly. Gradient-based optimization methods were utilized to adjust the tuning parameters to reconcile the frequency response of the mathematical model with that of experimental wind tunnel data. The final mathematical model is a linear, time-invariant state-space model which can be used in the design of aeroelastic flight control laws.

8.1 Future Work

Future work would be helpful in extending three aspects of this study.

First, the experimental data on which the mathematical modeling was based can be improved upon. With modern optical and laser-based mode-shape measurement systems, authoritative mode shape data can be obtained which can augment or even supercede the finite-element model in modeling structural dynamics. Higher quality sensors (such as accelerometers) which are electronically shielded from outside electrical interference could also eliminate significant sources of uncertainty in the initial model, increasing its accuracy.

The mathematical modeling itself could be improved by applying global optimization methods, since it has been demonstrated that there is potential for improvement from an optimization method which can circumvent local minima. The mathematical modeling could also be improved by modeling more damping mechanisms such as static and dynamic friction

at the wing root and load-dependent damping.

Lastly, this mathematical model can be tested in active aeroservoelastic control law design. Future work may include synthesis and testing of gust load alleviation, maneuver load alleviation, and flutter suppression control laws using this model. These control laws can then make viable more lightweight aircraft designs which have increased performance over designs with passive structures.

BIBLIOGRAPHY

- [1] J. G. Jones. Ride-bumpiness and the influence of active control systems. In *High-speed, Low-level Flight: Aircrew Factors*, AGARD-CP-228, October 1979.
- [2] Eli Livne. Aircraft active flutter suppression: State of the art and technology maturation needs. *Journal of Aircraft*, 55(1):410–452, 2018.
- [3] E. Nissim, A. Caspi, and I. Lottati. Application of the aerodynamic energy concept to flutter suppression and gust alleviation by use of active controls. Technical Note NASA TN D-8212, National Aeronautics and Space Administration, Langley Research Center Hampton, VA, United States, June 1976.
- [4] William E. Boeing Department of Aeronautics and Astronautics. 3x3 low-speed wind tunnel, 2023. <https://www.aa.washington.edu/AERL/3x3>.
- [5] Jake D. Quenzer, Alison Zongolowicz, Kimberly A. Hinson, Bijan Barzgaran, Eli Livne, Mehran Mesbahi, and Kristi Morgansen. *Model for Aeroelastic Response to Gust Excitation*. American Institute of Aeronautics and Astronautics Inc., 2019.
- [6] John M. Riebe. A correlation of two-dimensional data on lift coefficient available with blowing-, suction-, slotted-, and plain-flap high-lift devices. Research Memorandum NACA-RM-L55D29a, National Advisory Committee for Aeronautics, Langley Aeronautical Lab. Langley Field, VA, United States, October 1955.
- [7] Kenneth L. Roger. Airplane math modeling methods for active control design. In *Structural Aspects of Active Controls*, AGARD-CP-228, August 1977.
- [8] O. Sensburg, J. Becker, H. Lusebrink, and F. Weiss. Gust load alleviation on airbus a 300. In *13th Congress of the International Council of the Aeronautical Sciences, and AIAA Aircraft Systems and Technology Conference*, pages 44–58, Seattle, WA, 1982.
- [9] Siemens. *Aeroelastic Analysis User's Guide*. Siemens Digital Industries Software, 2020.2 edition, 2020.
- [10] Theodore Theodorsen. General theory of aerodynamic instability and the mechanism of flutter. Technical Memorandum NACA-TR-496, National Advisory Committee for Aeronautics, Langley Aeronautical Lab. Langley Field, VA, United States, January 1949.

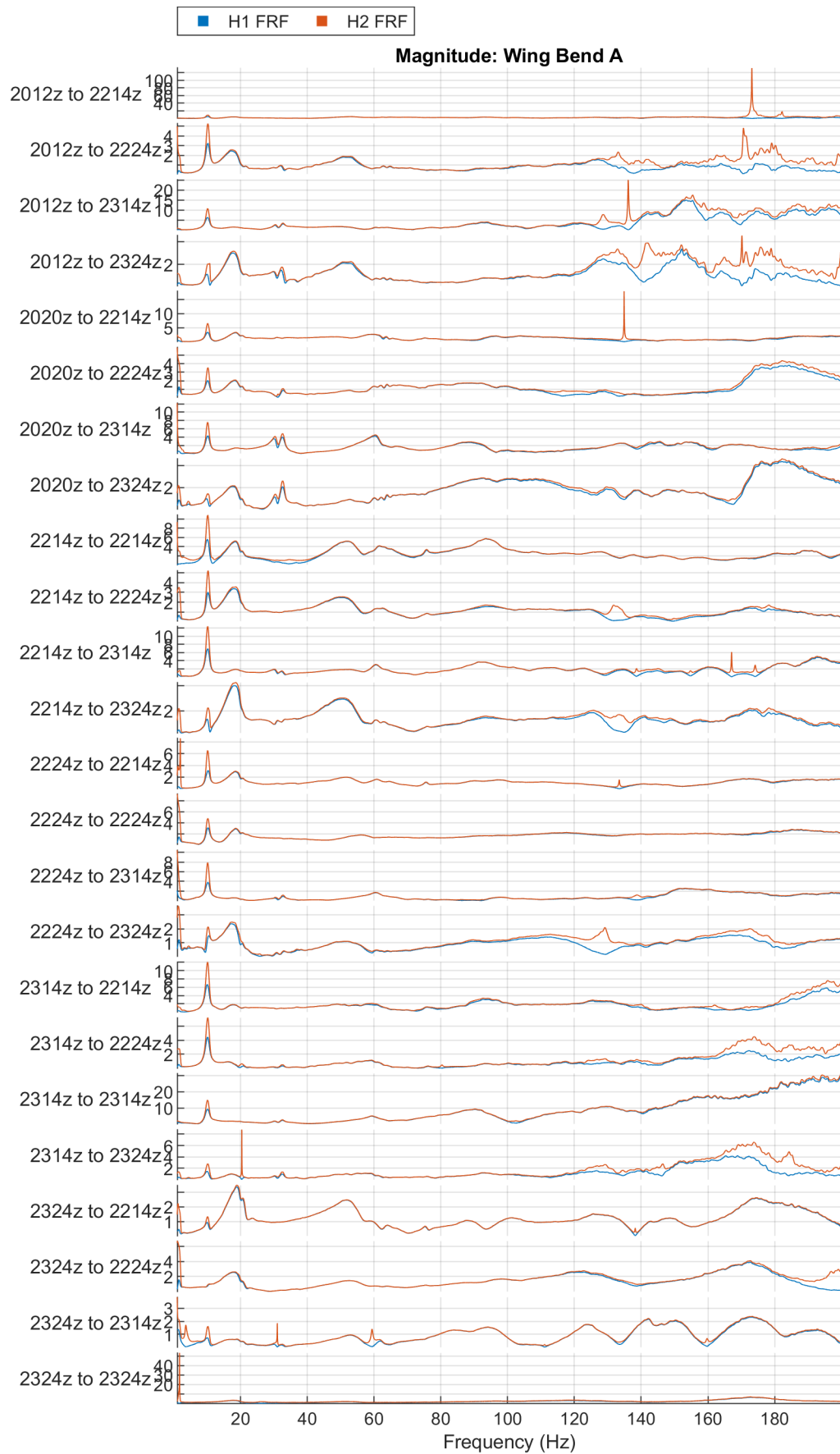
- [11] Mark B. Tischler and Robert K. Remple. *Aircraft and Rotorcraft System Identification*, chapter 7. American Institute of Aeronautics and Astronautics, Inc., 1801 Alexander Bell Drive, Reston, VA 20191-4344, 2 edition, 2006.
- [12] A. D. Young. The aerodynamic characteristics of flaps. Reports and Memoranda 2622, Ministry of Supply, February 1947.

Appendix A

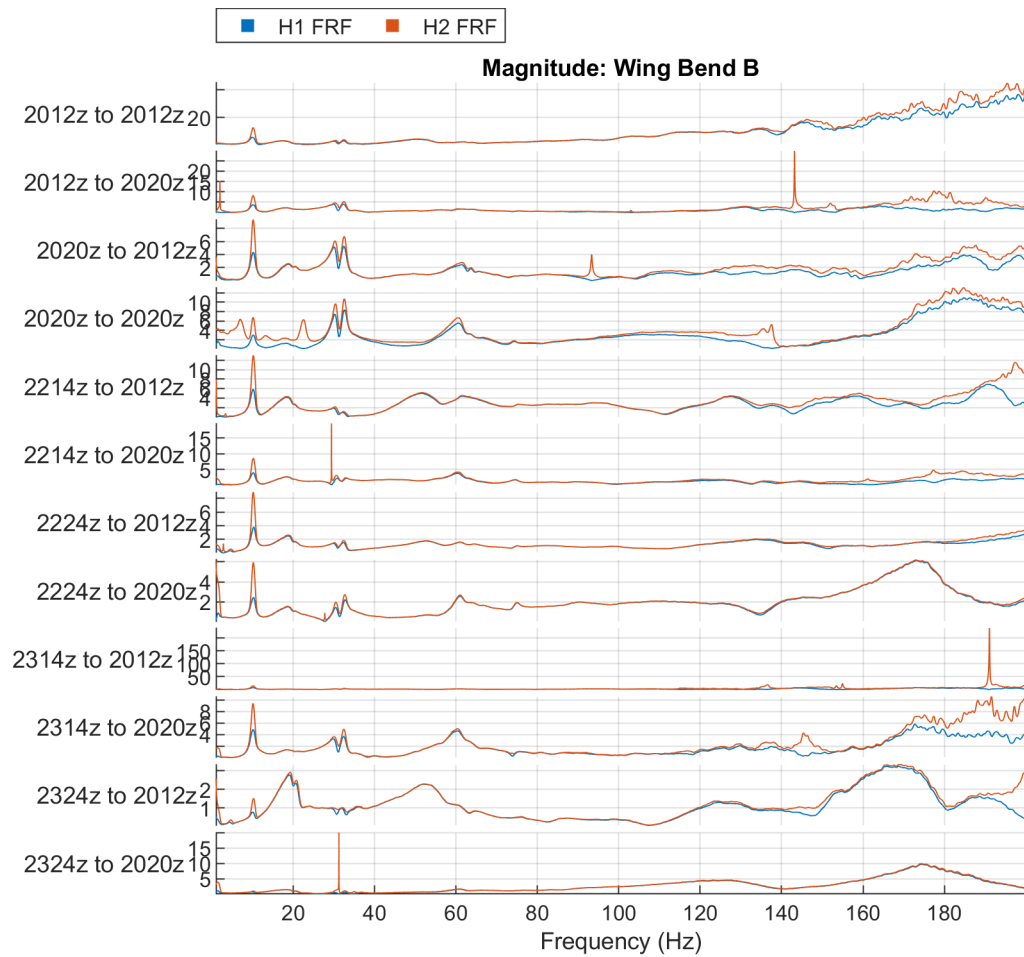
FREQUENCY RESPONSE PLOTS

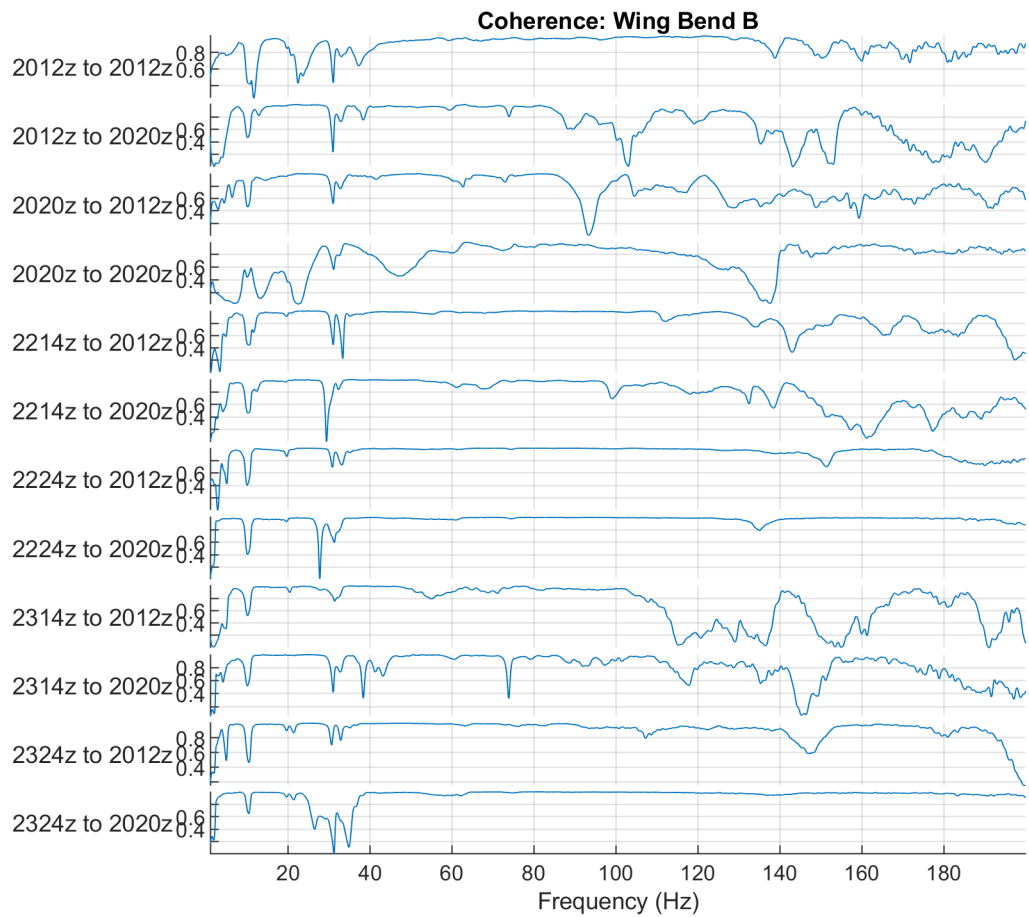
A.1 *Ground Vibration Testing*

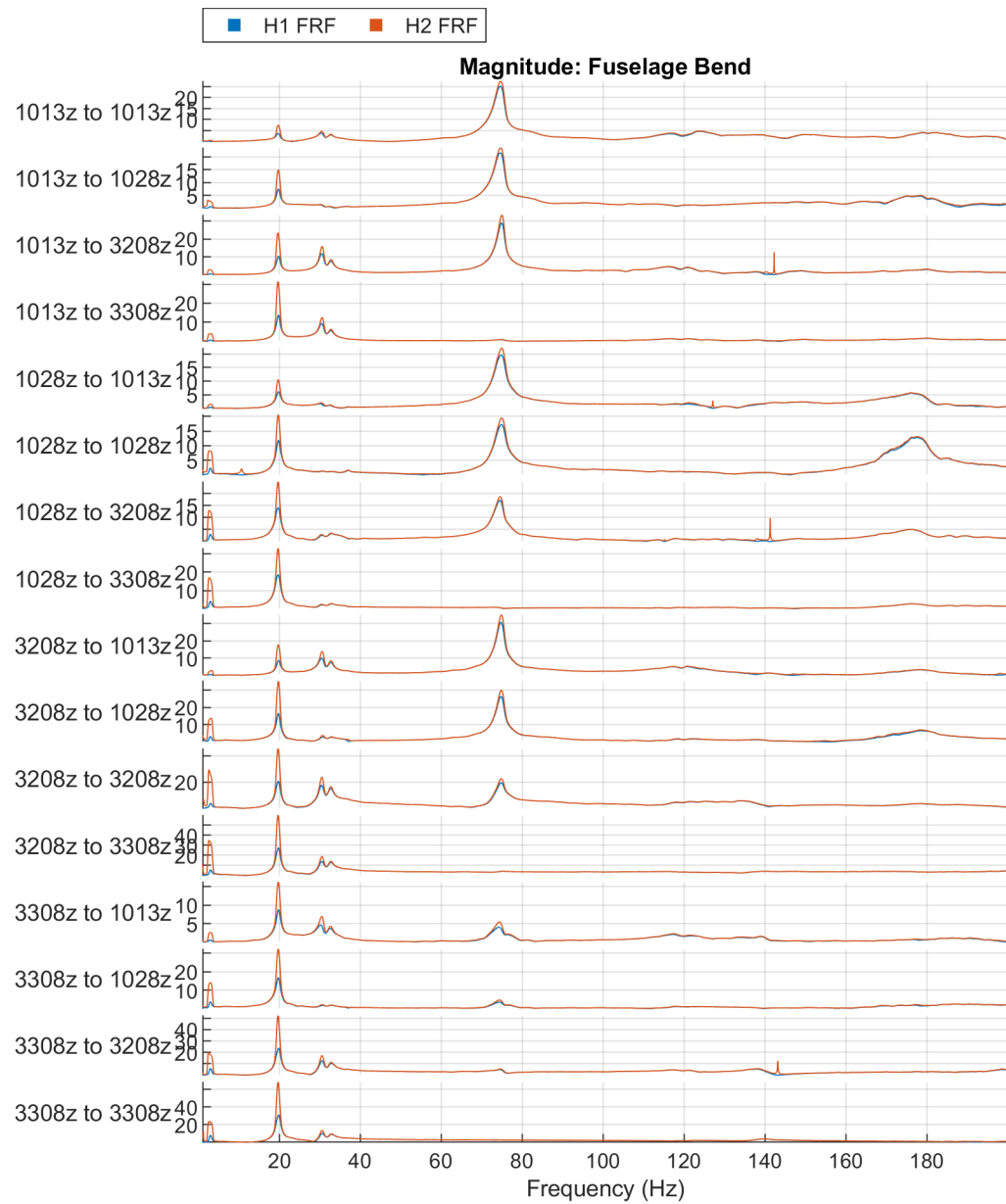
The plots each indicate the acceleration response at a location to an impulse input at a location. The locations are labeled by node number and direction. The locations of the respective nodes can be found in Figure 5.1.

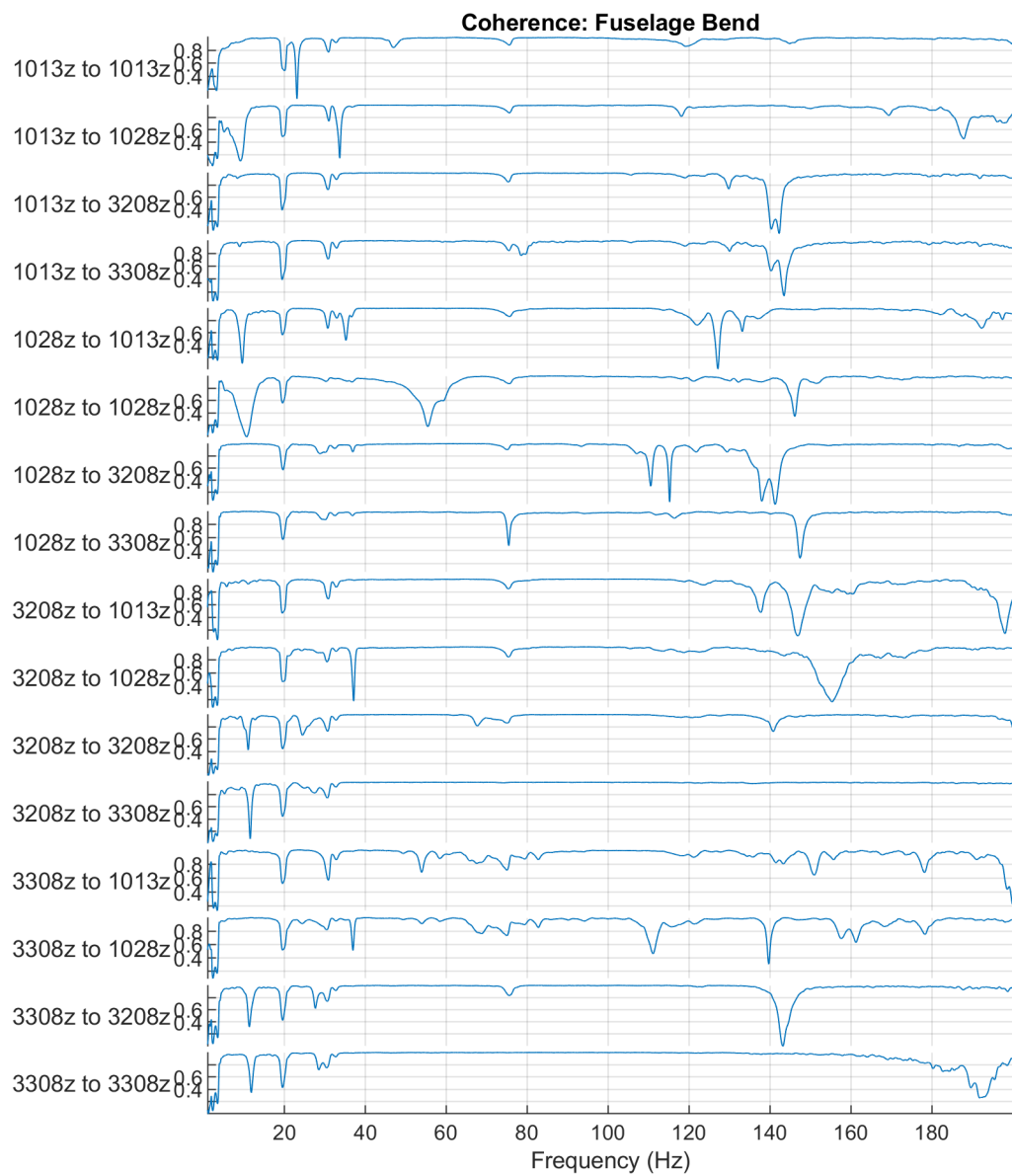


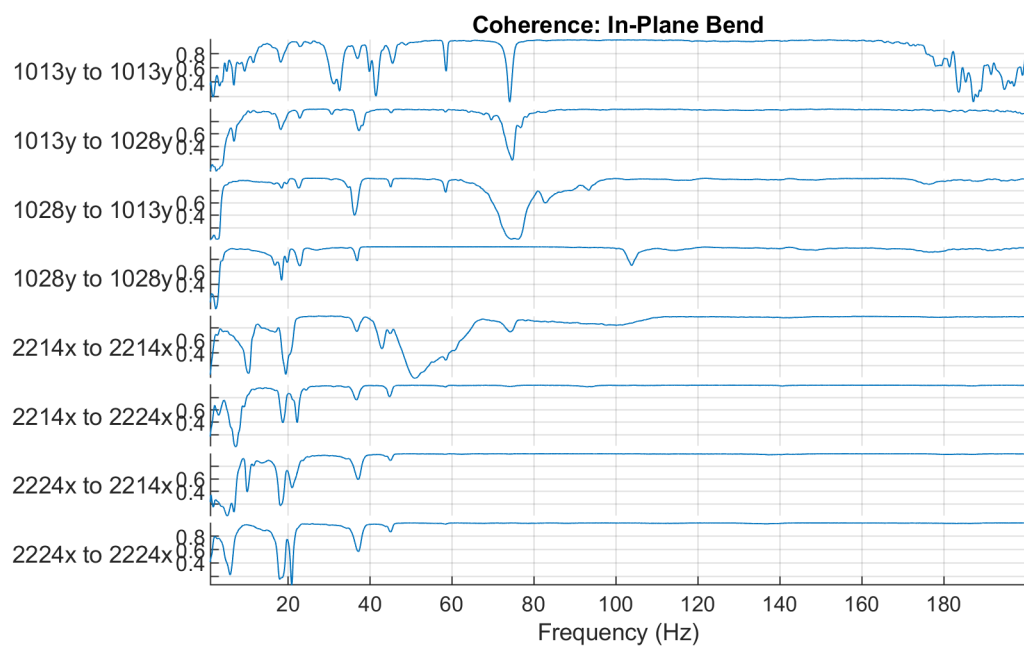
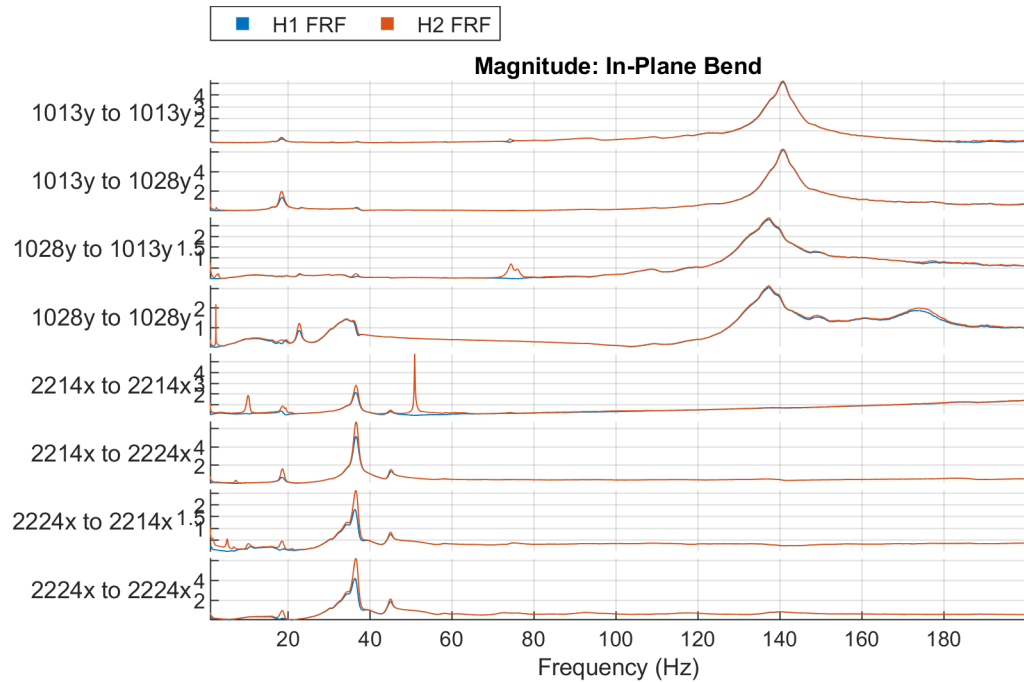


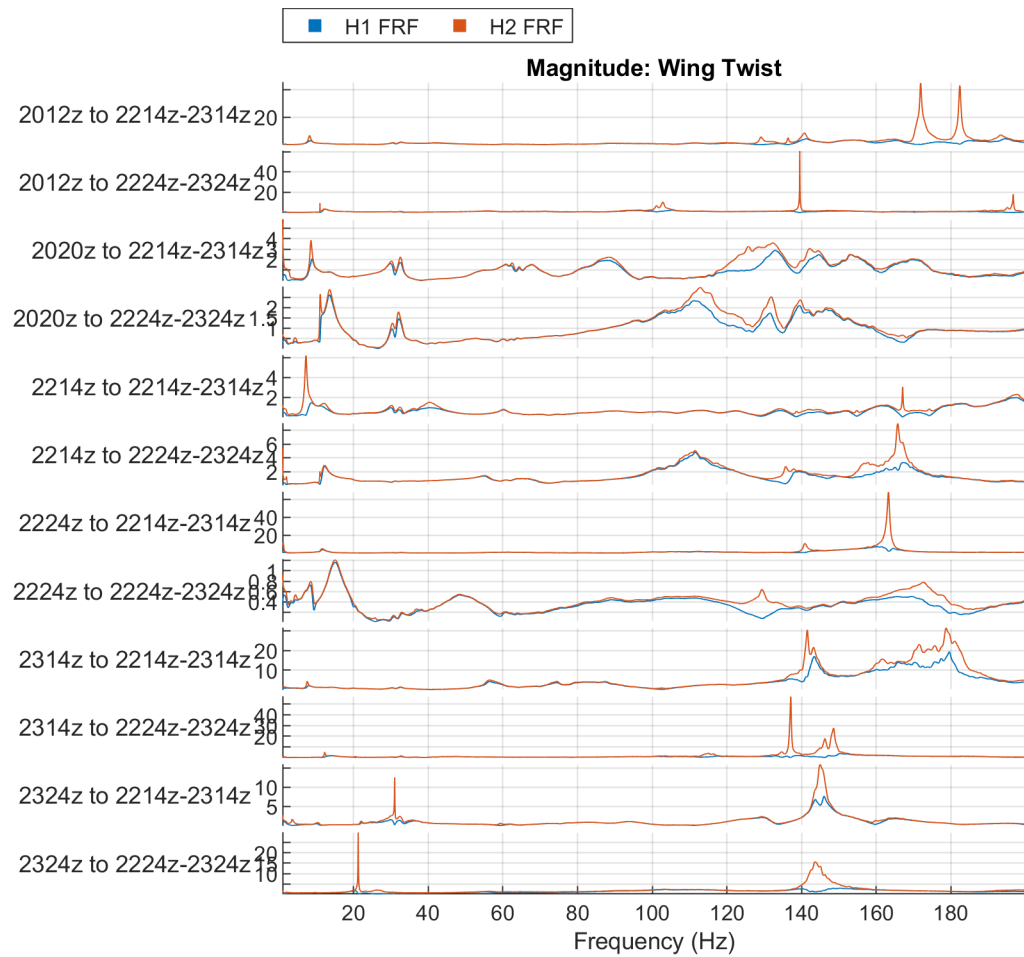


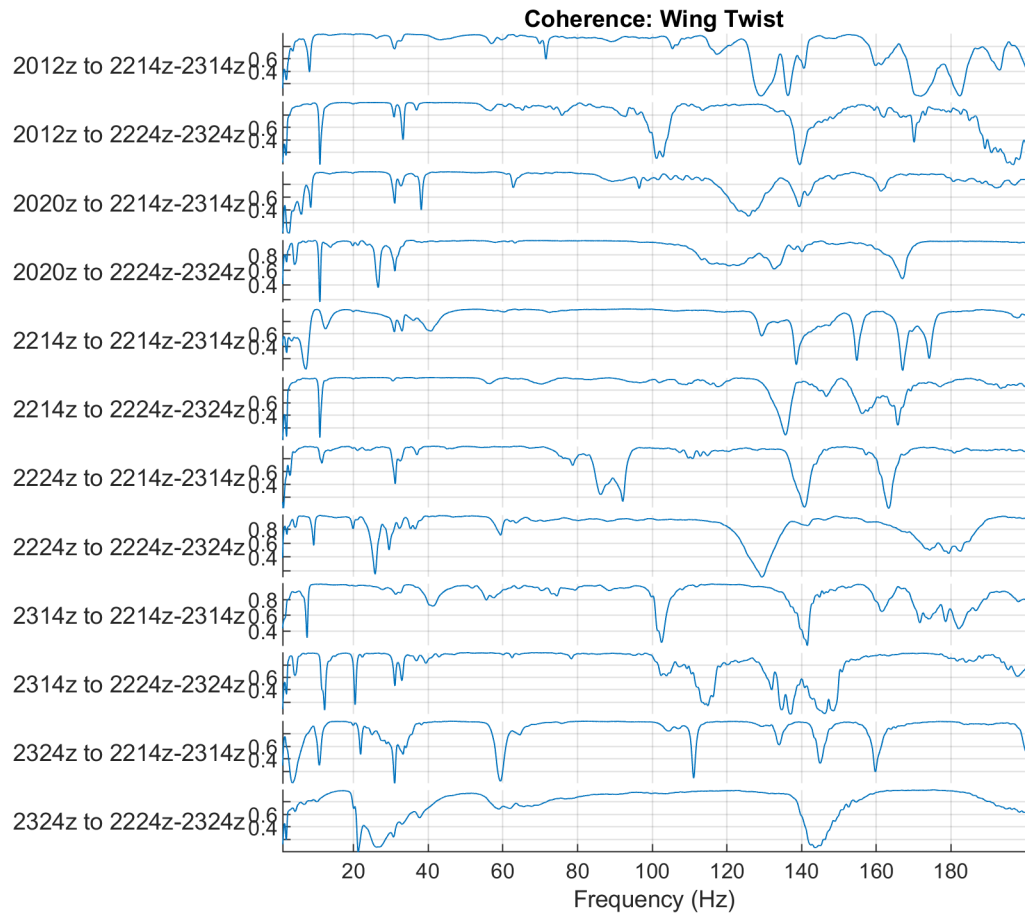






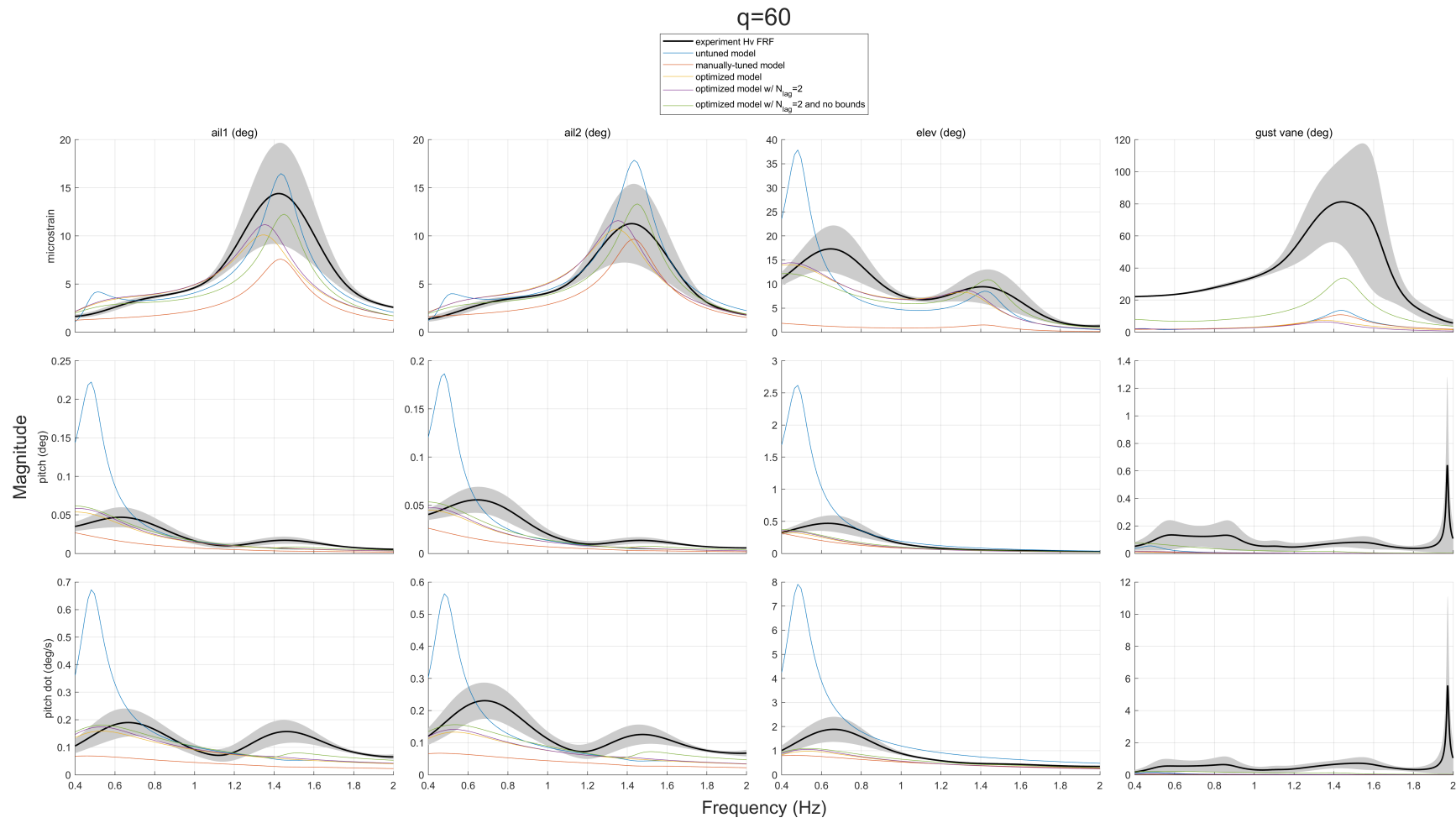


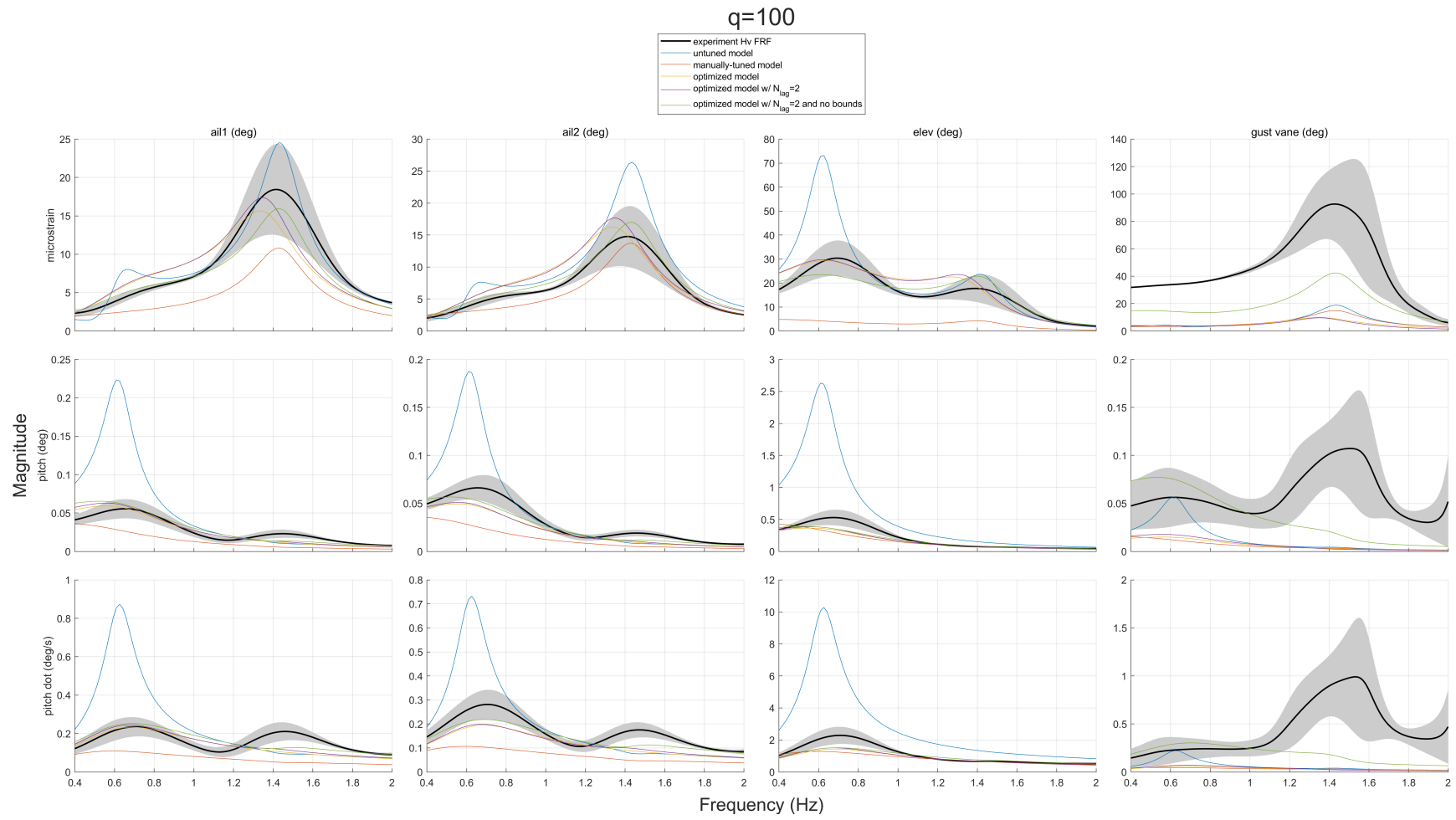


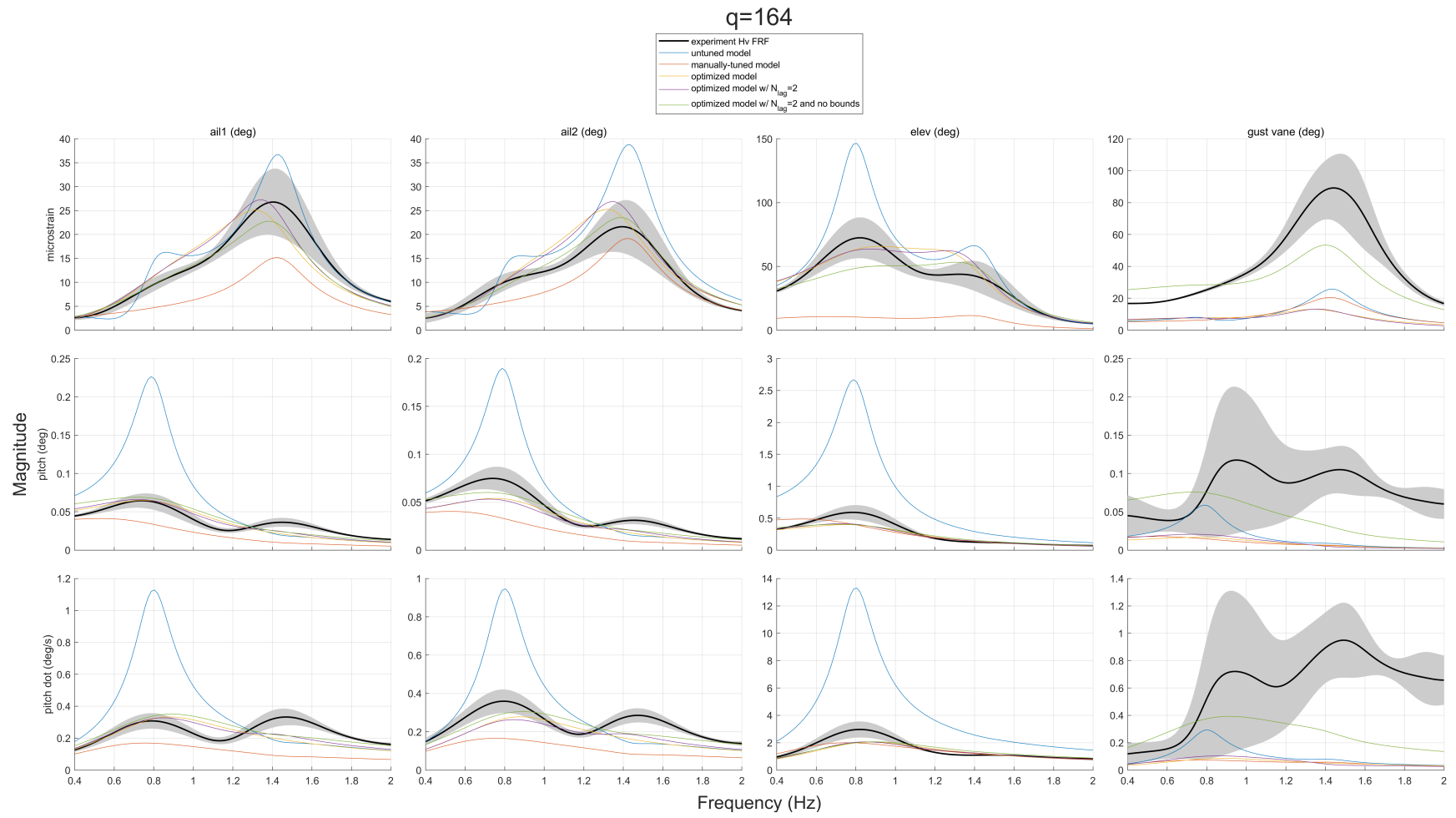


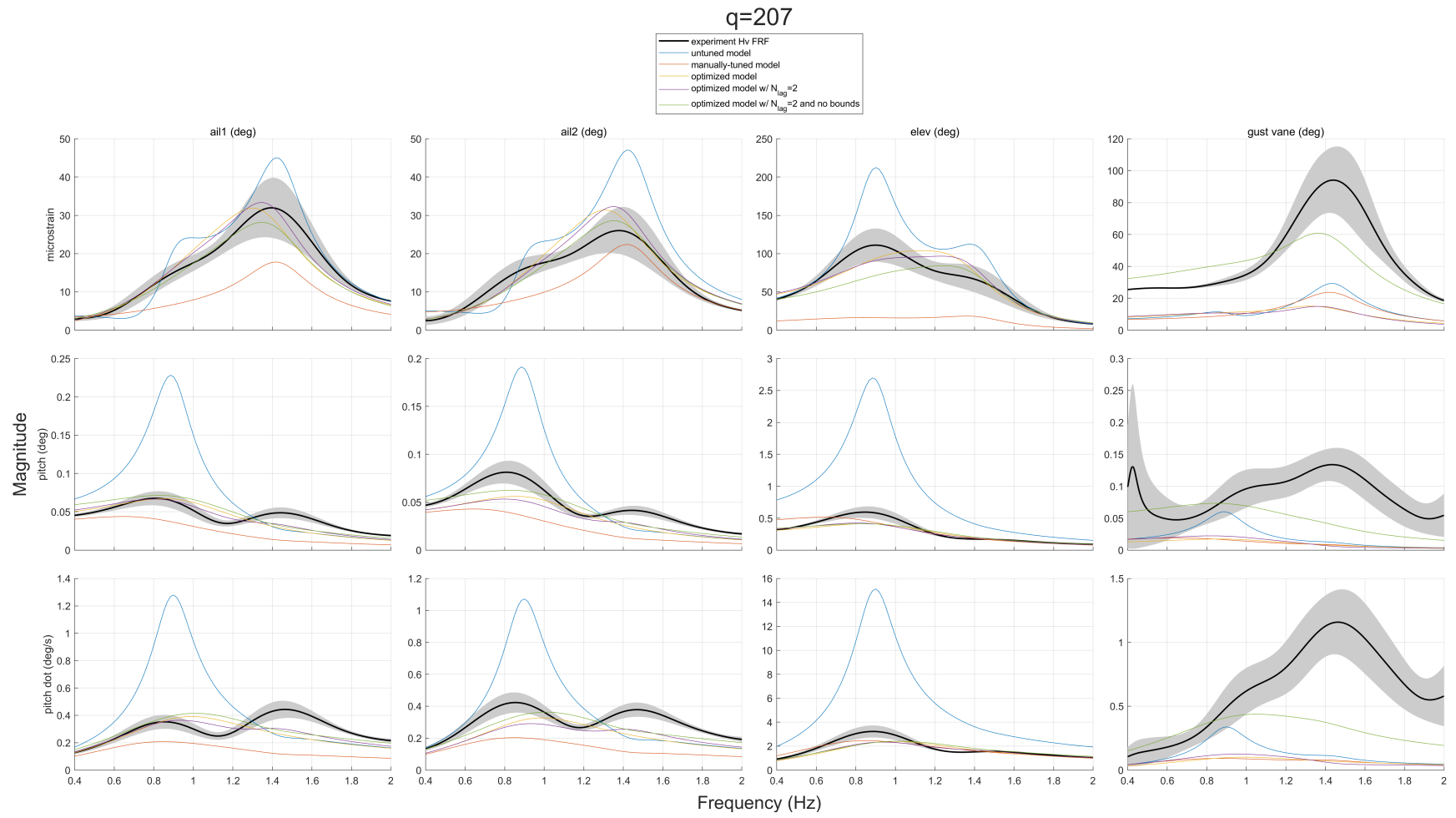
A.2 Wind Tunnel Testing and Mathematical Models

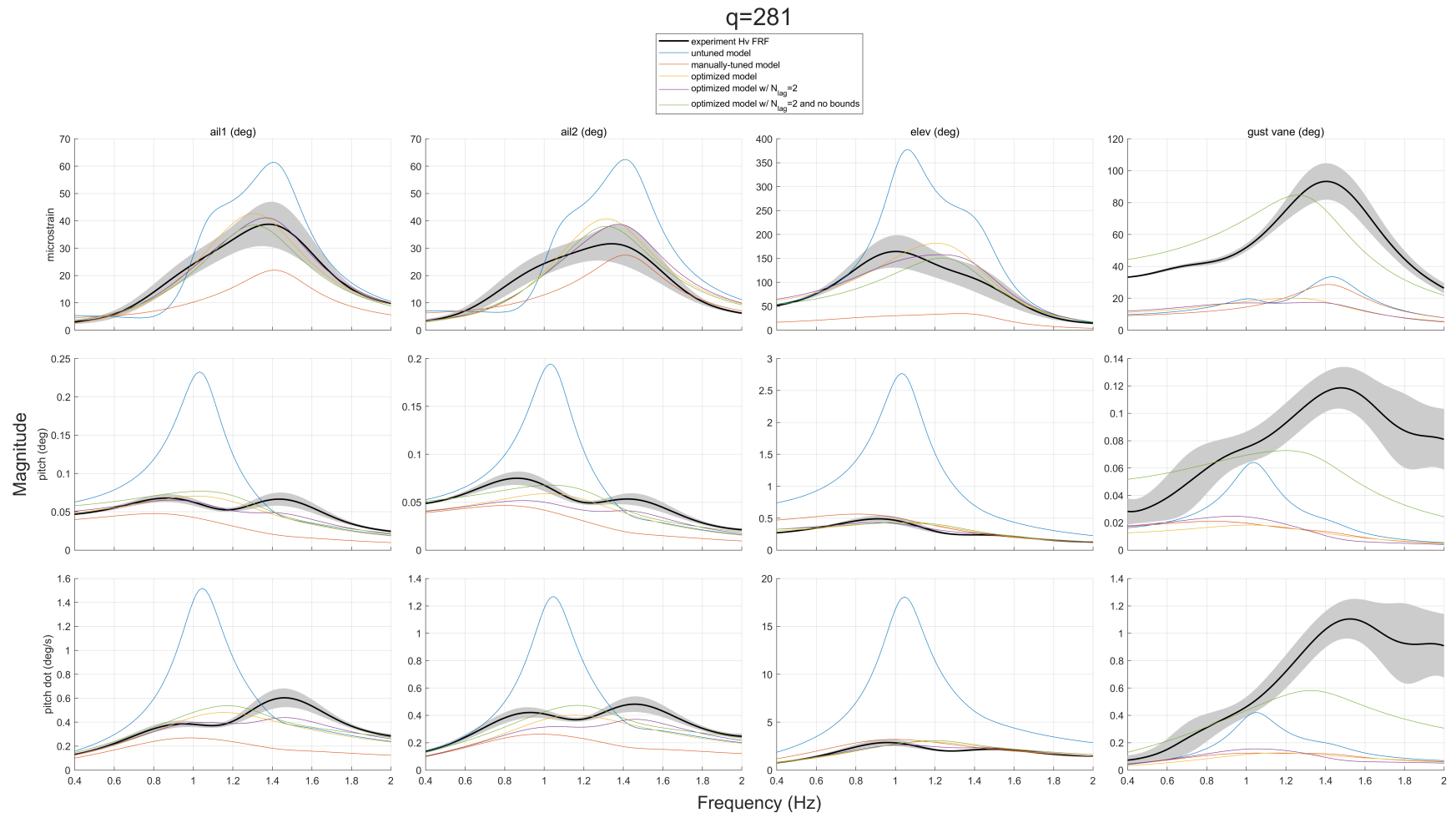
Unless otherwise noted, mathematical models demonstrated in this section have $n_s = 2$, $N_{\text{lag}} = 0$, and physically bounded tuning variables as defined in Table 7.3

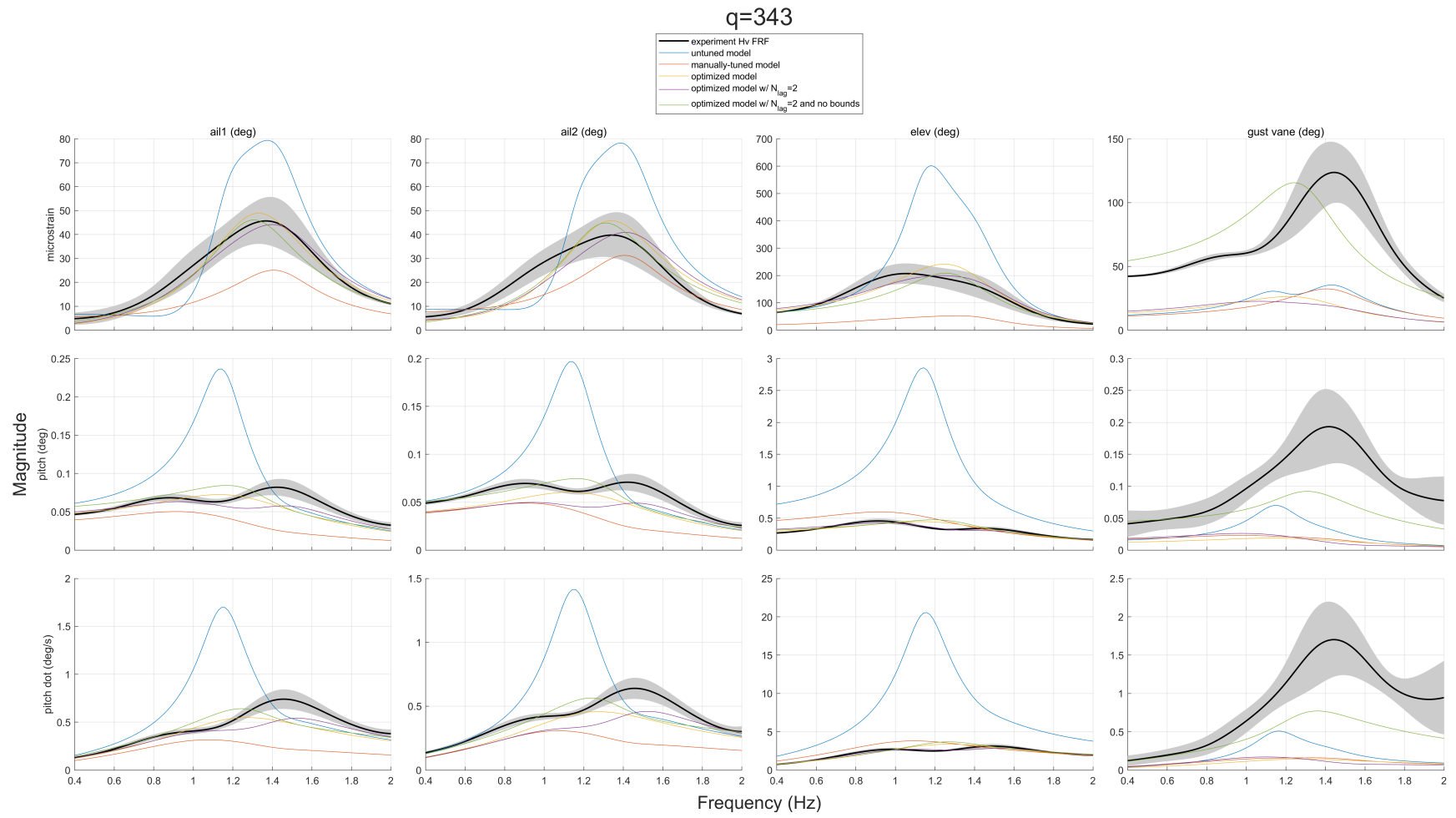












Appendix B

OPTMODEL

This model has $n_s = 2$ structural dynamic modes and $N_{\text{lag}} = 2$ lag terms in the Roger approximation. The model's state vector is thus determined to have 16 entries, corresponding to two states, two rates, two two-element lag states, and four two-element actuator states.

$$s\{x\} = [A]\{x\} + [B]\{u\}$$

$$\{y\} = [C]\{x\} + [D]\{u\}$$

$$\{u\} = \begin{Bmatrix} \text{aileron 1 (deg)} \\ \text{aileron 2 (deg)} \\ \text{elevator (deg)} \\ \text{gust vanes (deg)} \end{Bmatrix} \quad \{y\} = \begin{Bmatrix} \text{acceleration 1 (g)} \\ \text{acceleration 2 (g)} \\ \text{acceleration 3 (g)} \\ \text{strain}(\mu\varepsilon) \\ \text{rotation (deg)} \\ \text{rotation rate (deg/s)} \end{Bmatrix}$$

$$[A] = \begin{bmatrix} 0 & 0 & 1 & 0 & 0 & 0 & 0 & 0 & 0 & 0 & 0 & 0 & 0 & 0 & 0 & 0 \\ 0 & 0 & 0 & 1 & 0 & 0 & 0 & 0 & 0 & 0 & 0 & 0 & 0 & 0 & 0 & 0 \\ -8.364 & 1.0122 & -2.9798 & -1.2393 & 50.8427 & -1.0236 & 50.8427 & -1.0236 & 0.2894 & 272.0845 & 0.28238 & 226.0819 & 3.918 & 1895.4093 & 18.1004 & 700.7528 \\ 31.1331 & -72.347 & 0.16671 & -2.6834 & -0.09316 & 52.6318 & -0.09316 & 52.6318 & -0.83246 & -1066.5187 & -1.5058 & -1130.5021 & -0.0066816 & -3.2323 & -993.5842 & -117723.7787 \\ 0 & 0 & 0.0037325 & 0.00010307 & -10.9181 & 0 & 0 & -10.9181 & 0 & 0 & 0.0058316 & 0 & 0.0032023 & 0 & 0.018892 & 0 \\ 0 & 0 & 0.0016017 & 0.0016552 & 0 & -10.9181 & 0 & 0 & -0.012932 & 0 & 0 & -0.0020412 & 0 & 2.3027e-06 & 0 & 7236.2386 & 425661.0967 \\ 0 & 0 & 0.073988 & 0.13364 & 0 & 0 & -43.6726 & 0 & 0 & -0.23309 & 0 & 0 & -0.15955 & 0 & -0.77141 & 0 & -1672.7635 & -98397.8538 \\ 0 & 0 & 0.012592 & 0.1943 & 0 & 0 & 0 & -43.6726 & 1.2508 & 0 & 0.84331 & 0 & -9.373e-05 & 0 & -32449.5405 & -1908796.5027 \\ 0 & 0 & 0 & 0 & 0 & 0 & 0 & 0 & -62.2 & -1461 & 0 & 0 & 0 & 0 & 0 & 0 & 0 & 0 \\ 0 & 0 & 0 & 0 & 0 & 0 & 0 & 0 & 1 & 0 & 0 & 0 & 0 & 0 & 0 & 0 & 0 & 0 \\ 0 & 0 & 0 & 0 & 0 & 0 & 0 & 0 & 0 & 0 & 0 & -62.2 & -1461 & 0 & 0 & 0 & 0 & 0 \\ 0 & 0 & 0 & 0 & 0 & 0 & 0 & 0 & 0 & 0 & 1 & 0 & 0 & 0 & 0 & 0 & 0 & 0 \\ 0 & 0 & 0 & 0 & 0 & 0 & 0 & 0 & 0 & 0 & 0 & 0 & -62.2 & -1461 & 0 & 0 & 0 & 0 & 0 \\ 0 & 0 & 0 & 0 & 0 & 0 & 0 & 0 & 0 & 0 & 0 & 0 & 1 & 0 & 0 & 0 & 0 & 0 \\ 0 & 0 & 0 & 0 & 0 & 0 & 0 & 0 & 0 & 0 & 0 & 0 & 0 & -176.4706 & -10380.6228 \\ 0 & 0 & 0 & 0 & 0 & 0 & 0 & 0 & 0 & 0 & 0 & 0 & 0 & 0 & 1 & 0 & 0 & 0 \end{bmatrix}$$

$$[B] = \begin{bmatrix} 0 & 0 & 0 & 0 \\ 0 & 0 & 0 & 0 \\ -7.485e-05 & -6.7806e-05 & -0.00053481 & 0.0018052 \\ 0.0002643 & 0.00030513 & 9.1138e-07 & 0.25513 \\ 0 & 0 & 0 & -0.035782 \\ 0 & 0 & 0 & -0.71568 \\ 0 & 0 & 0 & 0.16544 \\ 0 & 0 & 0 & 3.2093 \\ -0.017453 & 0 & 0 & 0 \\ 0 & 0 & 0 & 0 \\ 0 & -0.017453 & 0 & 0 \\ 0 & 0 & 0 & 0 \\ 0 & 0 & -0.017453 & 0 \\ 0 & 0 & 0 & 0 \\ 0 & 0 & 0 & 0.017453 \\ 0 & 0 & 0 & 0 \end{bmatrix}$$

$$[C] = \begin{bmatrix} -4.4678 & 10.5555 & 0.003672 & 0.40351 & -0.46442 & -7.6763 & -0.46442 & -7.6763 & 0.11884 & 153.1878 & 0.21724 & 162.964 & -0.035862 & -17.3488 & 144.925 & 17184.8658 \\ -4.7205 & 10.5885 & -0.085971 & 0.36633 & 1.065 & -7.7089 & 1.065 & -7.7089 & 0.12758 & 161.4101 & 0.22579 & 169.8046 & 0.081999 & 39.6682 & 145.5045 & 17210.087 \\ -1.3058 & 0.15672 & -0.46543 & -0.19363 & 7.9415 & -0.15887 & 7.9415 & -0.15887 & 0.045188 & 42.4782 & 0.044078 & 35.2916 & 0.61198 & 296.0565 & 2.8082 & 107.1983 \\ 2.3726e-06 & 10070.1875 & 0 & 0 & 0 & 0 & 0 & 0 & 0 & 0 & 0 & 0 & 0 & 0 & 0 & 0 & 0 & 0 \\ 127.9694 & -0.0046878 & 0 & 0 & 0 & 0 & 0 & 0 & 0 & 0 & 0 & 0 & 0 & 0 & 0 & 0 & 0 & 0 \\ 0 & 0 & 127.9694 & -0.0046878 & 0 & 0 & 0 & 0 & 0 & 0 & 0 & 0 & 0 & 0 & 0 & 0 & 0 & 0 \end{bmatrix}$$

$$[D] = \begin{bmatrix} -3.7893e-05 & -4.3921e-05 & 4.8952e-06 & -0.037274 \\ -4.0154e-05 & -4.5971e-05 & -1.1193e-05 & -0.037228 \\ -1.1686e-05 & -1.0585e-05 & -8.3536e-05 & 0.00028686 \\ 0 & 0 & 0 & 0 \\ 0 & 0 & 0 & 0 \\ 0 & 0 & 0 & 0 \end{bmatrix}$$

∞